Long-Pentraxin 3 Derivative as a Small-Molecule FGF Trap for Cancer Therapy

A LONG-PENTRAXIN 3 DERIVATIVE AS THE FIRST SMALL MOLECULE FGF-TRAP FOR CANCER THERAPY

Roberto Ronca[1,8,*], Arianna Giacomini[1,8], Emanuela Di Salle[1], Daniela Coltrini[1], Katiuscia Pagano[2], Laura Ragona[2], Sara Matarazzo[1], Sara Rezzola[1], Daniele Maiolo[3], Rubben Torrella[4], Elisabetta Moroni[4], Roberta Mazzieri[5], Giulia Escobar[6], Marco Mor[7], Giorgio Colombo[4,*], Marco Presta[1,*]

Affiliations:

[1]Department of Molecular and Translational Medicine, University of Brescia, 25123 Brescia, Italy.

[2]NMR Laboratory, Istituto per lo Studio delle Macromolecole, CNR, 20133 Milan, Italy

[3]Chemistry for Technologies Laboratory and INSTM, School of Engineering, University of Brescia, 25123 Brescia, Italy

[4]Istituto di Chimica del Riconoscimento Molecolare, CNR, 20133 Milan, Italy

[5]University of Queensland Diamantina Institute, Translational Research Institute, Brisbane, Queensland 4102, Australia

[6]San Raffaele Telethon Institute for Gene Therapy, and Vita Salute San Raffaele University, 20132 Milan, Italy.

[7]Department of Pharmacology, University of Parma, 43121 Parma, Italy.

[8]These authors contributed equally to this work

*Correspondence: marco.presta@unibs.it; giorgio.colombo@icrm.cnr.it; roberto.ronca@unibs.it

Running title: PTX3-derived FGF-trap blocks tumor growth

SUMMARY

The fibroblast growth factor (FGF)/FGF receptor (FGFR) system plays a crucial role in cancer by affecting tumor growth, angiogenesis, drug resistance and escape from anti-angiogenic anti-vascular endothelial growth factor therapy. The soluble pattern recognition receptor long-pentraxin 3 (PTX3) acts as a multi-FGF antagonist. Here we demonstrate that human PTX3 overexpression in transgenic mice driven by the *Tie2* promoter inhibits tumor growth, angiogenesis and metastasis in heterotopic, orthotopic and autochthonous FGF-dependent tumor models. Next, pharmacophore modeling of the interaction of a minimal PTX3-derived FGF-binding pentapeptide with FGF2 is used for the identification of the first small molecule chemical (NSC12) which acts as an extracellular FGF trap with significant implications in cancer therapy.

SIGNIFICANCE

The FGF/FGFR system is an attractive target for cancer therapy. To date, only small molecule inhibitors targeting the tyrosine kinase or extracellular domains of FGFRs have been developed. Here we show that *Tie2* promoter-driven overexpression of human PTX3 in transgenic mice inhibits tumor growth and metastasis in heterotopic, orthotopic and autochthonous FGF-dependent tumor models. These observations set the basis for pharmacophore modeling and identification of a PTX3-derived small molecule, NSC12, acting as an extracellular FGF trap. Parenteral and oral delivery of NSC12 inhibits FGFR activation, tumor growth, angiogenesis and metastasis in FGF-dependent murine and human tumor models. NSC12 represents the first small molecule ligand trap that can be developed with therapeutic significance in cancer therapy.

HIGHLIGHTS

- hPTX3 overexpression blocks tumor growth and metastases in transgenic mice
- Pharmacophore modeling identified a PTX3-derived anti-FGF small molecule (NSC12)
- NSC12 inhibits FGF-dependent tumor growth, angiogenesis and metastases
- NSC12 acts as an small molecule FGF trap in cancer therapy

INTRODUCTION

Fibroblast growth factors (FGFs) are heparin-binding polypeptides produced by stromal and parenchymal tumor cells and readily sequestered into the extracellular matrix by heparan sulfate proteoglycans (HPSGs). FGFs bind tyrosine kinase (TK) FGF receptors (FGFR1-4), leading to the formation of signaling HSPG/FGF/FGFR ternary complexes (Beenken and Mohammadi, 2009). Activation of the FGF/FGFR system by gene upregulation, oncogenic mutations or amplifications is implicated in key steps of tumor growth and progression (Beenken and Mohammadi, 2009). Also, compensatory upregulation of the FGF/FGFR system may facilitate the escape from angiostatic anti-vascular endothelial growth factor (VEGF) blockade (Casanovas et al., 2005; Lieu et al., 2011). Thus, experimental and clinical evidence provides a compelling biologic rationale for the development of anti-FGF/FGFR targeting agents in cancer therapy.

Thus far two major classes of FGFR inhibitors have been developed: small molecule intracellular TK inhibitors and extracellular anti-FGFR antibodies or peptides (Ho et al., 2014). However, FGFR redundancy, limited selectivity and significant toxicity of TK inhibitors, and proteinaceous origin of extracellular FGFR antagonists may represent significant drawbacks for the development of novel anti-cancer drugs. An alternative/complementary approach may derive from the observation that FGFs are highly expressed in certain human tumors and exert paracrine/autocrine functions on cancer epithelial/stromal cells (Brooks et al., 2012), thus providing druggable targets for the development of "two-compartment" anti-FGF agents (Dieci et al., 2013), as hypothesized for soluble "decoy" FGFRs (Harding et al., 2013; Ho et al., 2014), heparin derivatives and polysulphated/polysulphonated compounds (Presta et al., 2005). However, the possibility to develop small organic molecules as extracellular multi-FGF ligand traps remains unexplored.

The soluble pattern recognition receptor long pentraxin-3 (PTX3) is produced by endothelial and immune cells in response to inflammatory signals (Garlanda et al., 2005). PTX3 binds various FGFs *via* its *N*-terminal extension, including FGF2, FGF6, FGF8b, FGF10 and FGF17, and inhibits FGF-dependent angiogenic responses (Camozzi et al., 2006; Leali et al., 2011; Presta et al., 2007; Ronca et al., 2013a). Accordingly, the acetylated pentapeptide Ac-ARPCA-NH_2 (in single letter code, hereafter referred to as ARPCA), corresponding to the *N*-terminal amino acid sequence PTX3(100-104), acts as a minimal anti-angiogenic FGF-binding peptide able to interfere with FGF/FGFR interaction (Leali et al., 2010). Thus, PTX3 represents a natural multi-FGF trap with potential implications for tumor therapy.

Indeed, PTX3-overexpressing FGF-dependent tumor cells show a reduced angiogenic and tumorigenic potential (Leali et al., 2011; Ronca et al., 2013a; Ronca et al., 2013b).

Here, we generated transgenic mice in which the expression of human *PTX3* is driven by the *Tie2* promoter and we demonstrate that hPTX3 overexpression inhibits FGF-dependent tumor growth, angiogenesis and metastasis in these mice. On this basis, pharmacophore modeling of ARPCA/FGF2 interaction was used to identify a small molecule [4,4,4-trifluoro-1-(3-hydroxy-10,13-dimethyl-2,3,4,7,8,9,11,12,14,15,16,17-dodecahydro-1H-cyclopenta[a]phenanthren-17-yl)-3-(trifluoromethyl)butane-1,3-diol; named NSC12] that acts as an extracellular FGF trap. Parenteral and gavage delivery of NSC12 inhibits FGFR activation, tumor growth, angiogenesis and metastasis in various FGF-dependent murine and human tumor models.

RESULTS

Generation of transgenic hPTX3-expressing TgN(Tie2-hPTX3) mice.

To mimic the effect of a local/systemic delivery of hPTX3 on tumor growth, we generated transgenic TgN(Tie2-hPTX3) mice expressing hPTX3 under the control of the endothelial specific *Tie2/Tek* transcription regulatory sequences. hPTX3 is expressed in various organs of these mice where it accumulates in the perivascular/stromal microenvironment (**Figure 1A-B**), leading to a significant increase of hPTX3 serum levels (105 ± 20 ng/ml *versus* < 1.8 ng/ml in transgenic and wild-type animals, respectively).

As anticipated, lung endothelial cells isolated from TgN(Tie2-hPTX3) animals showed impaired FGFR1 activation following stimulation by FGF2 when compared to wild-type cells (**Figure 1C**). Also, aorta rings harvested from TgN(Tie2-hPTX3) mice and embedded in fibrin gel in the presence of FGF2 showed a reduced capacity to form endothelial cell sprouts, retaining a full response to VEGF-A (**Figure 1D**). Finally, the angiogenic activity of FGF2 was significantly reduced in a subcutaneous (s.c.) Matrigel plug assay performed in TgN(Tie2-hPTX3) animals (**Figure 1E**). Notably, constitutive hPTX3 expression does not result in apparent defects in embryonic and post-natal development and in body weight gain; adult animals are fertile with no histological alterations of all tissues examined, including heart, liver, lungs and kidney (data not shown). Also, no significant changes in the expression levels of PTX3-targeted FGFs, including *Fgf2*, *Fgf6*, *Fgf8*, *Fgf10* and *Fgf17* (Ronca et al., 2013a), was observed in different organs of TgN(Tie2-hPTX3) mice when compared to wild-type animals (**Figure S1A**).

***Tie2* promoter-driven expression of hPTX3 impairs heterotopic tumor growth and neovascularization.**

TRAMP-C2 cells are a prototypic prostate carcinoma model driven by autocrine, androgen-upregulated FGF2 and FGF8b (Ronca et al., 2013a). To assess the impact of hPTX3 overexpression on the early phases of FGF-dependent tumor growth, we performed a short-term experiment in which TRAMP-C2 cells embedded in alginate plugs were injected s.c. in male TgN(Tie2-hPTX3) mice. After 2 weeks, alginate pellets grafted in transgenic animals showed a significant reduction of FGFR1 phosphorylation when compared to plugs implanted in wild-type animals, providing the first experimental evidence about the capacity of transgenic hPTX3 overexpression to disrupt ligand-dependent FGFR activation *in vivo* (**Figure 2A-B**). Accordingly, tumor cell proliferation rate and vascularization were drastically impaired in TRAMP-C2 plugs grafted in TgN(Tie2-hPTX3) mice (**Figure 2C**) with a significant inhibition of TRAMP-C2 tumor growth in a long term s.c. assay (**Figure 2D**).

A significant reduction of tumor growth was observed in TgN(Tie2-hPTX3) mice also after s.c. injection of FGF-dependent B16-F10 melanoma cells or Lewis lung carcinoma (LLC) cells, a model in which the FGF/FGFR axis is associated with tumor growth and resistance to anti-VEGF therapy (Shojaei et al., 2009) (**Figure 2D**). Notably, no difference in the rate of tumor growth occurred in TgN(Tie2-hPTX3) animals grafted with FGF-independent TC-1 or C3 cancer cells (Accardi et al., 2014) (**Figure S2A**). Similarly, hPTX3 overexpression did not affect the growth of FGFR1-TRAMP-C2 lesions transduced with a constitutively activated form of the intracellular FGFR1 TK domain (Hart et al., 2000) and characterized by a faster rate of growth when compared to parental TRAMP-C2 tumors (**Figure S2B**).

At variance, hPTX3 overexpression inhibited the growth, proliferation rate and vascularization of experimental liver metastases after i.v. injection of M5076 reticulum cell sarcoma cells (Talmadge and Hart, 1984) (**Figure 2F-G**). A similar inhibition was observed for the growth of B16-F10 melanoma lung metastases (**Figures 2H-I**) that occurred in the absence of any effect of hPTX3 expression on B16-F10 cell homing to the lungs (**Figure S2C**). In contrast, no difference in lung colonization was observed between wild-type and TgN(Tie2-hPTX3) animals following i.v. injection of FGF-independent TC-1 cells (**Figure S2D**). Together, these data support the notion that the anti-tumor effect of hPTX3 is related to its extracellular inhibitory action on the autocrine/paracrine loops of stimulation triggered by the FGF/FGFR system in FGF-dependent tumors.

Tie2-expressing monocytes (TEMs), a bone marrow (BM)-derived cell population homing the tumor microenvironment, may act as cell shuttles for a tumor-targeted delivery of anti-cancer therapeutics (De Palma et al., 2007). On this basis, we generated chimeric mice by immunodepletion of wild-type animals followed by reconstitution with the BM harvested from TgN(Tie2-hPTX3) or control GFP-expressing transgenic TgN(Tie2-GFP) mice (**Figure S3A-B**). As shown in **Figure 2E**, myeloid cell-mediated delivery of hPTX3 by TEMs infiltrating the s.c. TRAMP-C2 tumors (**Figure S3C**) caused a significant delay of tumor growth in chimeric TgN(Tie2-hPTX3) BM-transplanted mice when compared with tumors grafted in TgN(Tie2-GFP) BM-transplanted animals. The inhibitory effect was paralleled by a significant reduction of tumor cell proliferation but not of tumor vascularization (**Figure S3D-E**), possibly as a consequence of the lower local and systemic concentration of hPTX3 produced by transplanted myeloid cells compared to hPTX3 transgenic animals.

Tie2 **promoter-driven hPTX3 production impairs orthotopic and autochthonous multistage tumor growth.**

Next, we evaluated the effect of stroma-derived hPTX3 on the growth of syngeneic murine pancreatic and mammary carcinoma cells orthotopically grafted in TgN(Tie2-hPTX3) mice. When compared to wild-type animals, intra-pancreatic injection of Panc02 tumor cells in TgN(Tie2-hPTX3) mice resulted in a significant reduction of tumor burden and enhancement of animal survival (**Figure 3A**). Similarly, a significant delay in the appearance of mammary tumor nodules, decreased tumor growth, and increased survival time were observed in female TgN(Tie2-hPTX3) mice with respect to control animals after transplantation of syngeneic EO771 breast carcinoma cells into the mammary fat pad (**Figure 3B**).

Transgenic adenocarcinoma of the mouse prostate (TRAMP) mice represent an autochthonous multistage model of prostate cancer in which the FGF/FGFR system plays a relevant role (Polnaszek et al., 2003). To further assess the anti-neoplastic potential of the FGF trap activity of hPTX3, the prostatic tumor progression in double transgenic TgN(Tie2-hPTX3)/TRAMP mice was compared to the progression in age-matched TRAMP animals at 10 and 12 weeks of age. Quantitative histological analysis revealed a lower incidence of well-differentiated/moderately-differentiated tumors (**Figure 3C**) and a reduction of $Ki67^{+}$ tumor cells (**Figure 3D**) in TgN(Tie2-hPTX3)/TRAMP mice, index of significant delay of prostatic tumor progression in hPTX3-expressing mice. This effect was transient and was not observed at later stages of tumor progression in which poorly differentiated/neuroendocrine tumors arise (data not shown), possibly due to compensatory

mechanisms that overcome FGF inhibition by PTX3. Even though further experiments will be required to assess the mechanisms able to overcome PTX3-mediated oncosuppressive effects, the data clearly show that PTX3 can delay, at least transiently, the progression of prostate cancer in the TRAMP model.

Homozygous *Ptx3* inactivation enhances FGF-dependent angiogenesis, tumor growth and metastasis.

Homozygous null (*Ptx3*$^{-/-}$) mice develop normally and do not show any gross abnormality, even though *Ptx3*$^{-/-}$ females are subfertile. PTX3 deficiency causes a reduced immune response to pathogens and increases tissue damage in ischemic myocardium and atherosclerotic lesions [see (Daigo et al., 2014) for a more detailed description of the *Ptx3*$^{-/-}$ mouse phenotype]. Also, recent observations have shown that the growth of chemical carcinogen-induced skin tumors is delayed in these animals (Bonavita et al., 2015). To further evaluate the impact of PTX3 on tumor growth, we compared the angiogenic activity of FGF2 protein and the tumorigenic and metastatic activity of melanoma B16-F10 cells when assessed in syngeneic *Ptx3*$^{-/-}$ mice *versus* wild-type and TgN(Tie2-hPTX3) animals. As shown in **Figure 3E**, *Ptx3* knockout results in a significant increase of both basal and FGF2-triggered angiogenic responses in the Matrigel plug assay when compared to those observed in TgN(Tie2-hPTX3) and wild-type animals. It must be pointed out that the s.c. injection of Matrigel induces *per sè* a mild pro-inflammatory reaction, leading to the co-expression within the plug of PTX3 and FGF2, thus explaining the effect of *Ptx3* knockout on the basal neovascular response in this assay (Leali et al., 2012). In agreement with these observations, the tumorigenic and metastatic activities of B16-F10 cells were significantly enhanced in *Ptx3* null animals in respect to wild-type and hPTX3-overexpressing mice (**Figure 3F-G**). Thus, PTX3 appears to act as a natural brake of FGF-mediated angiogenesis, tumor growth and metastasis. This inhibitory activity is further enhanced by *Tie2* promoter-driven hPTX3 overexpression in tumor-bearing mice. These observations paved the way for the exploitation of the FGF trap activity of PTX3 in cancer therapy and for the development of novel PTX3-derived anti-FGF synthetic compounds.

Identification of a PTX3-derived small molecule FGF trap.

PTX3 is a 340 kDa protein composed of eight 381 amino acid protomers (Inforzato et al., 2010). The complex proteinaceous structure of PTX3 hampers its pharmacological exploitation. In this context, we identified the acetylated pentapeptide ARPCA as the minimal PTX3(100-104) amino acid sequence able to bind FGF2 and interfere with FGF2/PTX3 and HSPG/FGF2/FGFR1 interactions (Leali et al.,

2010). ARPCA acts as a potent FGF2 and FGF8b antagonist (Leali et al., 2010; Ronca et al., 2013a; Giacomini et al., 2015), representing a useful starting point for the rational identification of low molecular weight, nonpeptidic FGF antagonists.

On this basis, an atomistic model of the ARPCA/FGF2 complex was generated as the basis for the identification of the physico-chemical determinants required for productive ARPCA/FGF2 interaction. This information was translated into a pharmacophore model for the identification of drug-like hits *via* the screening of small molecule libraries (Colombo et al., 2010). First, the principal conformations populated by ARPCA in solution, derived from a 200ns-long explicit water molecular dynamics (MD) simulation, were subjected to multiple docking runs on the FGF2 surface, followed by MD refinement of the resulting complex (~100ns). The results (detailed in Supplementary Information) showed that ARPCA engages the FGF2 surface that faces the D2-D3 linker and D3 domain of FGFR (Plotnikov et al., 1999). The analysis of the statistical distribution of ARPCA/FGF2 interactions was consistent with previously published NMR-STD data, indicating that the peptide contacts FGF2 *via* the methyl groups of Ala1, Ala5 and of the acetyl capping group (Leali et al., 2010). Next, the ARPCA key functional groups, combined with the characterization of their relative space orientations, were used to build a pharmacophore model for the screening of the NCI2003 small molecule database containing ~$3x10^5$ compounds (Developmental Therapeutics Program NCI/NIH at http://dtp.nci.nih.gov).

Filtering of the resulting set according to the Lipinsky drug-likeness rules returned 25 compounds. Ten of them, made available from NCI, were subjected to a preliminary screening for their capacity to prevent the formation of HSPG/FGF2/FGFR1(IIIc) ternary complexes in a FGF2-mediated cell-cell adhesion assay. This assay is based on the capacity of FGFs to interact simultaneously *in trans* with HSPGs and FGFRs expressed on neighboring cells, thus causing FGF-mediated cell-cell adhesion (Richard et al., 1995); FGF antagonists hamper FGF-mediated intercellular adhesion by binding FGF and preventing its interaction with HSPGs and/or FGFRs (Leali et al., 2010). As shown in **Figure S4A**, the 480 Da compound 4,4,4-trifluoro-1-(3-hydroxy-10,13-dimethyl-2,3,4,7,8,9,11,12,14,15,16,17-dodecahydro-1H-cyclopenta[a]phenanthren-17-yl)-3-(trifluoromethyl)butane-1,3-diol (NSC172285, herewith named NSC12, **Figure 4A**) prevented the formation of the HSPG/FGF2/FGFR1 complex (IC_{50} ~10 μM, **Figure 4B**) whereas the other compounds were devoid of significant activity. On this basis, NSC12 was characterized further and the NSC21 compound was used as a negative control.

In a first set of experiments, NSC12 was investigated by surface plasmonic resonance (SPR) analysis for its capacity to prevent the binding of FGF2 to heparin immobilized to a BIAcore sensor chip or to an immobilized sFGFR1(IIIc)/Fc chimera. As shown in **Figure 4C**, NSC12 does not affect

FGF2/heparin interaction whereas it inhibits the binding of FGF2 to the immobilized receptor (ID_{50} ~30 μM). No effect was instead exerted by NSC21 on both sensor chips. Thus, as observed for PTX3/FGF2 and ARPCA/FGF2 complexes (Leali et al., 2010), NSC12 interferes with FGF2/FGFR1 interaction without affecting the ability of the growth factor to interact with heparin/HSPGs.

The capacity of NSC12 to bind to immobilized FGF2 was confirmed by SPR spectroscopy. The SPR binding isotherm (**Figure 4D**) shows a Langmuir-like shape for monovalent binding with a dissociation constant (K_d) equal to 51 ± 7 μM. The 1:1 stoichiometry of the FGF2:NSC12 interaction was confirmed also by surface density SPR measurements (Maiolo et al., 2012) performed at 100 μM NSC12 and showing that $1.28x10^{10}$ molecules/mm^2 of NSC12 bind to $1.45x10^{10}$ molecules/mm^2 of immobilized FGF2.

FGF2/NSC12 interaction was investigated also by the CONtact Angle MOlecular REcognition (CONAMORE) biosensor that probes the nanomechanical aspects of binding, complementing the information obtained by SPR (Maiolo et al., 2012). The CONAMORE binding isotherm performed on the same FGF2 chip used for SPR (**Figure 4D**) evidences that the onset of significant nanomechanical effects of FGF2 binding occurs at ~40 μM NSC12, consistent with the K_d calculated by SPR. In addition, no nanomechanical effect is registered when NSC12 is run onto a urea-denatured FGF2 chip (**Figure 4D**), further pointing to the specificity of the interaction.

Docking and MD simulations performed on NSC12/FGF2 system indicated that NSC12 and ARPCA, while sharing the same pharmacophoric points necessary to anchor FGF2, do not target entirely identical/overlapping regions on the FGF2 molecule, as expected given their different chemical nature and pharmacophore design. Indeed, besides engaging the FGF2 surface that faces the D2-D3 linker and D3 domain of FGFR, NSC12 further extends into the FGF2 region facing the FGFR D2 domain (D2), as detailed in Supplementary Information and in **Figure 4E**. On this basis and given that the D3 domain does not adopt a stable persistent three-dimensional fold in solution (Herbert et al., 2013), the D2 domain was used as a probe to investigate the overall effects of NSC12 on the FGF2/FGFR complex by NMR. Relaxation data demonstrate that NSC12 shifts the FGF2/D2 equilibrium towards the uncomplexed forms, as deduced from the decrease of the average ^{15}N transverse relaxation rate value measured for D2 and FGF2 upon NSC12 addition to the D2/FGF2 complex (Supplementary Information and **Figure S4B**).

Finally, when tested by SPR analysis on all canonical FGFs (Itoh and Ornitz, 2004), NSC12 binds also immobilized FGF3, FGF4, FGF6, FGF8, FGF16, FGF18, FGF20 and FGF22 with K_d values ranging

between ~16 and ~120 μM (**Figure 4F**). No apparent interaction was observed for the other FGFs tested, possibly because of the limited sensitivity of the method due to the low molecular weight of NSC12 and/or to the low efficiency of the immobilization procedure for some of the FGFs tested. On this basis, the capacity of NSC12 to affect the activity of FGFR1(IIIc)-binding FGFs and of FGFR2(IIIb)-binding FGFs (Zhang et al., 2006) was assessed by the HSPG/FGF/FGFR1 ternary complex assay described above and by a KATO III cell proliferation MTT assay (Bai et al., 2010), respectively. As shown in **Figure 4G-H,** NSC12 inhibits HSPG/FGF/FGFR ternary complex formation induced by FGFR1(IIIc)-binding FGF1, FGF4, FGF5, FGF6, FGF8, FGF9, FGF16, FGF17, FGF18 and FGF20 and the proliferative capacity of FGFR2(IIIb)-binding FGF3, FGF7, FGF10 and FGF22 in KATO III cells. Together with its FGF2 antagonist activity, these data indicate that NSC12 may act as a multi-FGF trap by interacting with all members of the canonical FGF subfamilies. In addition, when assessed for its ability to interact with hormonal FGFs, SPR analysis showed the capacity of NSC12 to bind FGF21 (Kd = 53±13 μM) but failed to detect a significant interaction with immobilized FGF19 or FGF23. However, when tested on MDA-MB-361 breast cancer cells, the compound was able to inhibit $ERK_{1/2}$ phosphorylation and the mitogenic response elicited by all hormonal FGFs in these cells (**Figure S4C**). Accordingly, NSC12 hampered FGF23-mediated FGFR1 activation in Klotho-expressing CHO cells (Urakawa et al. 2006) (**Figure S4D**).

NSC12 inhibits FGF-dependent angiogenesis and tumor cell proliferation.

In keeping with its capacity to antagonize FGF2/FGFR1 interaction, NSC12 inhibited FGFR1 phosphorylation in human umbilical vein endothelial cells (HUVECs) stimulated by FGF2 with a significant inhibition of HUVEC proliferation (IC_{50} ~6.5 μM) mainly due to their accumulation in the G_0/G_1 phase of the cell cycle (**Figures 5A-B**). Also, NSC12 inhibited the sprouting activity exerted by FGF2 on HUVEC spheroids embedded in fibrin gel (**Figure 5C**) and impaired the angiogenic response triggered by FGF2 in the chick embryo chorioallantoic membrane (CAM) assay (**Figure 5D**). NSC12 had no effect on the activity of VEGF-A in all these assays and control NSC21 was inactive. Thus, NSC12 acts as a selective anti-angiogenic FGF antagonist. Accordingly, the inhibitory activity exerted by NSC12 on endothelial cell proliferation, as well as on tumor cell proliferation (see below), was reversed by a molar excess of FGF2 (**Figure S5A**).

When challenged *in vitro* on tumor cell lines, NSC12 impaired the FGF-mediated proliferation of murine (TRAMP-C2) and human (LNCaP and DU145) prostate cancer cells where FGFR1 is a driver

of tumor growth and drug resistance (**Figure 5E**). Similar results were obtained for FGF-dependent murine (LLC) and human (H520) lung cancer cells characterized by *FGFR1* overexpression or amplification, respectively (**Figure 5F**). As observed for HUVECs, treatment with NSC12 caused the reduction of the S-phase of the cell cycle in all tumor cell lines but LLC cells, in which an accumulation in the S-phase was observed (**Figure 5E-F**). Control NSC21 was inactive in all the cell lines tested and no inhibitory effect was observed when FGF/FGFR-independent HCC827 lung cancer cells (harbouring a tumor-driving mutation of the EGFR TK domain) were challenged with NSC12 (**Figure 5F**).

The inhibitory activity of NSC12 was not restricted to FGFR1-dependent tumor cells. Indeed, the compound affected also the proliferation of FGFR2-dependent KATO III gastric carcinoma cells, FGFR3-dependent KMS-11 myeloma cells and FGFR4-dependent MDA-MB-361 breast cancer cells **(Figure S5B)**. Accordingly, NSC12 inhibited FGFR1, FGFR2, FGFR3, and FGFR4 phosphorylation in CHO cell transfectants (**Figure S5C**).

To define a therapeutically effective dose and to assess the FGF antagonist activity of NSC12 *in vivo*, TRAMP-C2 cells were embedded in alginate plugs and grafted s.c. in syngeneic male mice that were treated i.p. every other day for one week with increasing doses of NSC12 (from 2.5 to 10 mg/kg). As shown in **Figure 6A-C**, NSC12 caused a significant decrease of tumor weight, tumor cell FGFR1 phosphorylation and proliferation, and tumor $CD31^+$ neovascularization at all the doses tested whereas NSC21 was ineffective (**Figure 6A-C** and **Figure S6A**). Since the 10 mg/kg dose resulted in a partial body weight loss (**Figure S6B**), the 7.5 mg/kg dose was chosen for further experimentation. This dose was sufficient to fully inhibit FGFR1 phosphorylation in TRAMP-C2/alginate implants (**Figure 6D)** with no effect in two week-treated animals on body weight (**Figure S6B**), hematologic parameters and blood serum components (**Figure S6C**). Remarkably, NSC12 treatment did not affect serum concentration of endocrine FGFs, including FGF23 (**Figure S6D**).

On this basis, additional short-term assays were performed on FGF-dependent human cancer cells. To this aim, alginate plugs containing human prostate cancer (DU145) or lung cancer (H520) cells were injected s.c. in immunodeficient mice that were treated i.p. every other day with 7.5 mg/kg NSC12 or NSC21 for one week. As shown in **Figures 6E-F**, NSC12 caused a significant reduction of tumor weight and tumor $CD31^+$ neovascularization with a consequent increase of tumor cell death (as assessed by TUNEL staining). Notably, in keeping with *in vitro* observations, i.p. administration of NSC12 did not exert any effect *in vivo* on FGF-independent HCC827 tumor cells, causing only a

limited inhibition of the scarce neovascular response elicited by these cells (**Figure 6G**). Again, NSC21 was ineffective in all the alginate plugs tested.

Together, these data provide the first experimental evidence about the capacity of a small molecule FGF trap to disrupt FGF/FGFR signalling *in vivo*, leading to inhibition of tumor cell proliferation and neovascularization in FGF-dependent tumors.

Inhibition of tumor growth by parenteral and oral delivery of NSC12.

Based on the results described above, NSC12 was assessed for its capacity to inhibit the tumorigenic activity of FGF-dependent TRAMP-C2 cells and of human prostate DU145 and lung H520 tumor cells following i.p. administration in syngeneic and nude mice, respectively. To this purpose, tumor cells were injected s.c. and animals were randomly distributed in vehicle-, NSC12- or NSC21-treated groups when tumors were palpable. As shown in **Figure 7A**, NSC12 exerted a significant inhibitory effect on the growth of both murine and human tumor grafts whereas NSC21 was ineffective. Moreover, NSC12 inhibited the formation of experimental lung metastases after i.v. injection of B16-F10-*luc* cells (**Figure 7B**) and of spontaneous lung metastases induced by orthotopic grafting of breast carcinoma EO771 cells into the mammary fat pad followed by surgical removal of the primary tumor (**Figure 7C**). At variance, NSC12 did not affect the growth of FGF-independent TC-1 and C3 tumor grafts and of TRAMP-C2 and LLC lesions overexpressing the constitutively activated form of the intracellular FGFR1 TK domain, thus confirming the specificity of the effect (**Figure S7**).

Finally, to establish whether NSC12 may exert a significant anti-tumor activity also after oral administration, male mice were injected s.c. with TRAMP-C2 cells embedded in alginate plugs and treated by gavage with 7.5 mg/kg NSC12 or NSC21 for 4 days. Strikingly, gavage administration of NSC12 significantly impaired FGFR1 phosphorylation in TRAMP-C2 plugs when compared to plugs from animals treated with NSC21 or vehicle (**Figure 7D**). To confirm the oral activity of NSC12 also in human tumors, FGF-dependent H520 cells were grafted s.c. in nude mice. When tumors were palpable, animals were randomly distributed in 3 experimental groups and treated orally with 7.5 mg/kg NSC12 or NSC21 or vehicle. As shown in **Figure 7E**, gavage administration of NSC12 resulted in a significant inhibition of H520 tumor growth that was confirmed by measuring the end-stage tumor weight. This occurred in the absence of any effect of drug administration on body weight and survival of treated animals.

DISCUSSION

Here we demonstrate that *Tie2* promoter-driven hPTX3 overexpression in transgenic mice inhibits tumor growth, angiogenesis and metastasis in heterotopic, orthotopic and autochthonous FGF-dependent tumor models. On this basis, pharmacophore modeling of the interaction of the minimal PTX3-derived FGF-binding pentapeptide ARPCA with FGF2 was used for the identification of NSC12 as a small molecule FGF trap active by parenteral as well as by gavage administration in tumor-bearing mice.

Transgenic overexpression and myeloid cell-mediated delivery of hPTX3 inhibits FGF-dependent tumors

PTX3 binds various FGFs, thus exerting a FGF blocking activity. Here, we generated a transgenic TgN(Tie2-hPTX3) murine model in which *hPTX3* expression is driven by the *Tie2* promoter, leading to a significant increase of hPTX3 levels in perivascular microenvironment and in the bloodstream. hPTX3 overexpression hampers the tumorigenic, angiogenic and metastatic potential of various syngeneic FGF-dependent murine tumor cell lines following heterotopic and orthotopic transplantation in TgN(Tie2-hPTX3) mice. Conversely, homozygous *Ptx3* inactivation enhances FGF-dependent angiogenesis, tumor growth and metastasis. Also, in keeping with the role of the FGF/FGFR pathway in the autochthonous TRAMP model of prostate cancer (Polnaszek et al., 2003), double transgenic TgN(Tie2-hPTX3)/TRAMP mice show a significant delay in prostate neoplastic progression when compared to TRAMP animals. Furthermore, intratumor TEM-mediated delivery of hPTX3 causes a significant delay of TRAMP-C2 tumor growth in myelodepleted mice reconstituted with the BM from TgN(Tie2-hPTX3) animals.

Several pieces of evidence support the hypothesis that these oncosuppressive effects are due to the capacity of hPTX3 to act as a natural FGF trap. i) The endothelium of TgN(Tie2-hPTX3) mice shows a reduced response to FGF2 in various angiogenesis assays but retains a full capacity to respond to VEGF stimulation; ii) inhibition of FGFR1 phosphorylation occurs in FGF-dependent TRAMP-C2 cells grafted in TgN(Tie2-hPTX3) mice; iii) hPTX3 expression does not affect the growth of FGF-independent TC-1 or C3 tumors. We cannot rule out the possibility that PTX3 may have multiple impacts on tumor growth (Bonavita et al., 2015). Nevertheless, our data support the notion that the anti-tumor effects of hPTX3 are related to its inhibitory action on the autocrine/paracrine loops of stimulation triggered by the FGF/FGFR system in FGF-dependent tumors, setting the basis for the

identification of a PTX3-derived small molecule FGF trap. Clearly, at variance with FGFR blockers, PTX3 and PTX3-derived FGF traps are anticipated to be ineffective on tumors driven by ligand-independent FGFR activation, as shown for FGFR1-TRAMP-C2 cells grafted in TgN(Tie2-hPTX3) mice.

From a complex high molecular weight PTX3 protein to a small molecule FGF trap

PTX3 is a 340 kDa protein composed of 8 protomers held together by a complex disulfide bond network (Inforzato et al., 2010). ARPCA, corresponding to the amino acid sequence PTX3(100-104), represents the minimal FGF2-binding peptide able to antagonize FGF2 activity by interacting with the FGFR-binding region of the growth factor. These findings provided the bases for the design of a pharmacophore model of ARPCA/FGF2 interaction that was used for *in silico* screening of the NCI2003 small molecule database, thus allowing the identification of NSC12 as an ARPCA mimic. As anticipated, NSC12 binds FGF2 with a 1:1 stoichiometry and inhibits the formation of bioactive HSPG/FGF2/FGFR1 ternary complexes by inhibiting FGF2/FGFR interaction with no effect on FGF2/heparin interaction. Also, MD simulation-based studies of the FGF2/ARPCA and FGF2/NSC12 systems indicate that, because of the design process, both molecules may engage the FGF2 surface that faces the FGFR D3 domain and D2-D3 linker. Moreover, NSC12 further extends its interaction into the FGF2 region facing the FGFR D2 domain (**Figure 4E**). Accordingly, NMR relaxation data showed the ability of NSC12 to cause the dissociation of the FGF2/D2 complex. Even though further experiments involving the D2-D3 FGFR domains will be required to fully elucidate the inhibitory mechanism of NSC12, the combined MD, NMR, biochemical and biological data provide compelling evidence about the ability of the compound to act as a FGF antagonist.

Previous studies had identified the small molecule sm27 as a mimic of the FGF2-binding sequence of thrombospondin-1 able to engage the heparin-binding site of FGF2 (Pagano et al., 2012). As observed for other anionic compounds (Presta et al., 2005), sm27 may interact with the heparin-binding domain of a variety of signaling proteins with possible unsought side effects. At variance, the action of NSC12 appears to be restricted to FGF family members due to its direct effect on FGF/FGFR interaction with no effect on the heparin-binding VEGF-A_{165} isoform. Accordingly, NSC12 inhibits the proliferation of various FGF-dependent murine and human cancer cell lines with no inhibitory effect on HCC827 cancer cells that harbour a tumor-driving mutation of the EGFR TK domain and on FGF-independent cancer cell lines. Thus, NSC12 may act as a selective “two-compartment” epithelial-stromal targeting agent in FGF/FGFR-dependent tumors. Accordingly, i.p. and gavage administration of NSC12 hampers

FGFR phosphorylation, angiogenesis, primary and metastatic growth of FGF-dependent murine and human tumors in syngeneic and immunodeficient mice, respectively.

Therapeutic implications

The FGF/FGFR system is implicated in various steps of tumor growth and progression (Beenken and Mohammadi, 2009). Also, activation of the FGF/FGFR pathway is a mechanism of tumor escape in response to anti-VEGF therapies (Casanovas et al., 2005; Lieu et al., 2011). Thus, FGF blockade may represent a valid therapeutic option for selected tumors driven by an aberrant ligand-dependent FGFR activation (Dieci et al., 2013). However, the development of drugs specifically targeting the FGF/FGFR pathway proved to be difficult, also due to the high redundancy and pleiotropic effects of FGF and FGFR family members. Blockade of FGFR signaling by selective or broad-spectrum TK inhibitors has been associated with toxicity (Dieci et al., 2013) and a monoclonal antibody directed against FGFR1 has failed because of severe weight loss associated with hypothalamic binding (Sun et al., 2007). On the other hand, an allosteric multi-FGFR blocker with promising therapeutic implications has been recently described (Bono et al., 2013).

Drugs targeting FGF ligands may represent an interesting alternative to FGFR inhibitors. They include monoclonal antibodies and FGFR-derived decoy molecules acting as FGF traps (Harding et al., 2013; Ho et al., 2014). These molecules, however, are endowed with various limitations due to their proteinaceous origin. Our data demonstrate that NSC12 interacts with all members of the canonical FGF subfamilies involved in the growth of different human tumors (see **Table S1**). Moreover, NSC12 prevents FGF interaction with all four FGFRs. Thus, NSC12 represents the first small molecule multi-FGF trap with potential implications for cancer therapy. Of note, in keeping with the lack of pathological consequences following constitutive hPTX3 expression in transgenic mice, the anti-tumor action of NSC12 occurred in the absence of any systemic toxic effect in treated animals. In particular, at variance with the hyperphosphatemic effect of FGFR TK inhibitors in preclinical models (Brown et al., 2005) and cancer patients (Dieci et al., 2013), long-term administration of NSC12 did not affect the blood levels of phosphorus, calcium and FGF23. Also, RT-qPCR analysis did not show any change of *Fgf23* expression in kidneys and bone of NSC12-treated mice (data not shown). This occurred despite the capacity of NSC12 to affect the mitogenic activity of hormonal FGFs, including FGF23, when tested on MDA-MB-361 breast cancer cells. These observations are in keeping with the safety profile of the FGFR1-derived FGF trap FP-1039 (Harding et al., 2013) and of the allosteric multi-FGFR blocker SSR128129E (Bono et al., 2013). Together, these findings suggest that hyperphosphatemia

may represent a side effect of FGFR TK inhibitors rather than of extracellular inhibitors of the FGF/FGFR system. Given that both *FGF23* expression and activity are under the control of a complex mechanism of regulation that includes canonical, noncanonical and intracrine FGF/FGFR pathways (Martin et al. 2012; Han et al, 2015), further studies are required to elucidate this point.

Data from phase I/II clinical trials indicate that inhibition of the FGF/FGFR system may show antitumor activity and provide an incentive to develop novel, safer and more efficacious drugs (Dieci et al., 2013). NSC12 represents a lead compound for the development of orally active small molecule therapeutics for the treatment of tumors in which the ligand-dependent activation of the FGFR pathway is an oncogenic driver or is involved in the escape to conventional anti-cancer/anti-angiogenic therapies. Finally, from a broader perspective, our data emphasize the possibility to exploit protein interactome for the design of novel orally active small molecule multi-ligand traps with promising implications in cancer therapy.

EXPERIMENTAL PROCEDURES

Reagents and cell cultures. Reagents, recombinant proteins and cell line cultures are detailed in Supplementary Experimental Procedures.

NSC12 identification. Molecular dynamics simulations of ARPCA and NSC12, generation of a structural ARPCA-FGF2 complex model, pharmacophore model generation, screening process and parameters and NMR analysis are detailed in Supplemental Experimental Procedures**.**

Other assays. Standard protocols were used for cell proliferation, Western blotting, RT-PCR, immunostaining and other in vitro assay as detailed in Supplemental Experimental Procedures.

In vivo studies. Animal experiments were performed in accordance with the institutional and national guidelines and regulations. TgN(Tie2-hPTX3) mice were generated via lentiviral vector injection into the embryos. TRAMP mice were purchased from The Jackson Laboratory (Bar Harbor, ME, USA). Experimental conditions, tumor and metastasis assays and all procedures are described in Supplemental Experimental Procedures.

Statistical analyses. Statistical analyses were performed using the statistical package Prism 5 (GraphPad Software) as detailed in Supplemental Experimental Procedures. Differences were considered significant with $P < 0.05$.

CO-FIRST AUTHORS CONTRIBUTIONS

RR: conceived and performed *in vivo* experiments, analysed the data and wrote the manuscript; AG: conceived and performed *in vitro* experiments and histological analyses, analysed the data and revised the manuscript.

ACKNOWLEDGMENTS

This work was supported by grants from Ministero Istruzione, Università e Ricerca (FIRB project RBAP11H2R9 2011), Associazione Italiana Ricerca sul Cancro (AIRC grant n° 14395) to M.P. and from AIRC grant IG 15420 and Fondazione Cariplo (grant 2011.1800 "Premio Fondazione Cariplo per la Ricerca di Frontiera") to G.C. A.G. and S.M. were supported by Fondazione Italiana per la Ricerca sul Cancro Fellowships, E.D.S. by a Fondazione Veronesi Fellowship and K.P. by a Fondazione Antonio De Marco grant. NSC compounds were from Drug Synthesis and Chemistry Branch, Developmental Therapeutics Program, Division of Cancer Treatment and Diagnosis, National Cancer Institute (USA). The authors are grateful to C. Garlanda for providing $PTX3^{-/-}$ mice, B. Bottazzi, D. Moi, M. De Palma, L. Zetta and P. Bergese for helpful discussion and criticisms, and M. Belleri, M. Corsini, A. Bugatti and D. Leali for technical support. Conflict of interest disclosure: The authors declare no competing financial interests.

REFERENCES

Accardi, L., Paolini, F., Mandarino, A., Percario, Z., Di Bonito, P., Di Carlo, V., Affabris, E., Giorgi, C., Amici, C., and Venuti, A. (2014). In vivo antitumor effect of an intracellular single-chain antibody fragment against the E7 oncoprotein of human papillomavirus 16. Int. J. Cancer *134*, 2742-2747.

Bai, A., Meetze, K., Vo, N. Y., Kollipara, S., Mazsa, E. K., Winston, W. M., Weiler, S., Poling, L. L., Chen, T., Ismail, N. S., *et al*. (2010). GP369, an FGFR2-IIIb-specific antibody, exhibits potent antitumor activity against human cancers driven by activated FGFR2 signaling. Cancer Res. *70*, 7630-7639.

Beenken, A., and Mohammadi, M. (2009). The FGF family: biology, pathophysiology and therapy. Nat. Rev. Drug Discov. *8*, 235-253.

Bonavita, E., Gentile, S., Rubino, M., Maina, V., Papait, R., Kunderfranco, P., Greco, C., Feruglio, F., Molgora, M., Laface, I., *et al*. (2015). PTX3 is an extrinsic oncosuppressor regulating complement-dependent inflammation in cancer. Cell *160*, 700-714.

Bono, F., De Smet, F., Herbert, C., De Bock, K., Georgiadou, M., Fons, P., Tjwa, M., Alcouffe, C., Ny, A., Bianciotto, M., *et al*. (2013). Inhibition of tumor angiogenesis and growth by a small-molecule multi-FGF receptor blocker with allosteric properties. Cancer Cell *23*, 477-488.

Brooks, A. N., Kilgour, E., and Smith, P. D. (2012). Molecular pathways: fibroblast growth factor signaling: a new therapeutic opportunity in cancer. Clin. Cancer Res. *18*, 1855-1862.

Brown, A. P., Courtney, C. L., King, L. M., Groom, S. C., and Graziano, M. J. (2005). Cartilage dysplasia and tissue mineralization in the rat following administration of a FGF receptor tyrosine kinase inhibitor. Toxicol. Pathol. *33*, 449-455.

Camozzi, M., Rusnati, M., Bugatti, A., Bottazzi, B., Mantovani, A., Bastone, A., Inforzato, A., Vincenti, S., Bracci, L., Mastroianni, D., and Presta, M. (2006). Identification of an antiangiogenic FGF2-binding site in the N terminus of the soluble pattern recognition receptor PTX3. J. Biol. Chem. *281*, 22605-22613.

Casanovas, O., Hicklin, D. J., Bergers, G., and Hanahan, D. (2005). Drug resistance by evasion of antiangiogenic targeting of VEGF signaling in late-stage pancreatic islet tumors. Cancer Cell *8*, 299-309.

Colombo, G., Margosio, B., Ragona, L., Neves, M., Bonifacio, S., Annis, D. S., Stravalaci, M., Tomaselli, S., Giavazzi, R., Rusnati, M., *et al*. (2010). Non-peptidic thrombospondin-1 mimics as fibroblast growth factor-2 inhibitors: an integrated strategy for the development of new antiangiogenic compounds. J. Biol. Chem. *285*, 8733-8742.

Daigo, K., Mantovani, A., and Bottazzi, B. (2014). The yin-yang of long pentraxin PTX3 in inflammation and immunity. Immunol. Lett. *161*, 38-43.

De Palma, M., Murdoch, C., Venneri, M. A., Naldini, L., and Lewis, C. E. (2007). Tie2-expressing monocytes: regulation of tumor angiogenesis and therapeutic implications. Trends Immunol. *28*, 519-524.

Dieci, M. V., Arnedos, M., Andre, F., and Soria, J. C. (2013). Fibroblast growth factor receptor inhibitors as a cancer treatment: from a biologic rationale to medical perspectives. Cancer Discov. *3*, 264-279.

Garlanda, C., Bottazzi, B., Bastone, A., and Mantovani, A. (2005). Pentraxins at the crossroads between innate immunity, inflammation, matrix deposition, and female fertility. Annu. Rev. Immunol. *23*, 337-366.

Giacomini, A., Matarazzo, S., Pagano, K., Ragona, L., Rezzola, S., Corsini, M., Di Salle, E., Presta, M., and Ronca, R. (2015). A long pentraxin-3-derived pentapeptide for the therapy of FGF8b-driven steroid hormone-regulated cancers. Oncotarget. Epub ahead of print.

Han, X., Xiao, Z., and Quarles, LD. (2015). Membrane and integrative nuclear fibroblastic growth factor receptor (FGFR) regulation of FGF-23. J. Biol. Chem. *290*:10447-10459.

Harding, T. C., Long, L., Palencia, S., Zhang, H., Sadra, A., Hestir, K., Patil, N., Levin, A., Hsu, A. W., Charych, D., *et al*. (2013). Blockade of nonhormonal fibroblast growth factors by FP-1039 inhibits growth of multiple types of cancer. Sci. Transl. Med. *5*, 178ra139.

Hart, K. C., Robertson, S. C., Kanemitsu, M. Y., Meyer, A. N., Tynan, J. A., and Donoghue, D. J. (2000). Transformation and Stat activation by derivatives of FGFR1, FGFR3, and FGFR4. Oncogene *19*, 3309-3320.

Herbert, C., Schieborr, U., Saxena, K., Juraszek, J., De Smet, F., Alcouffe, C., Bianciotto, M., Saladino, G., Sibrac, D., Kudlinzki, D., *et al*. (2013). Molecular mechanism of SSR128129E, an extracellularly acting, small-molecule, allosteric inhibitor of FGF receptor signaling. Cancer Cell *23*, 489-501.

Ho, H. K., Yeo, A. H., Kang, T. S., and Chua, B. T. (2014). Current strategies for inhibiting FGFR activities in clinical applications: opportunities, challenges and toxicological considerations. Drug Discov. Today *19*, 51-62.

Inforzato, A., Baldock, C., Jowitt, T. A., Holmes, D. F., Lindstedt, R., Marcellini, M., Rivieccio, V., Briggs, D. C., Kadler, K. E., Verdoliva, A., *et al*. (2010). The angiogenic inhibitor long pentraxin PTX3 forms an asymmetric octamer with two binding sites for FGF2. J. Biol. Chem. *285*, 17681-17692.

Itoh, N., and Ornitz, D. M. (2004). Evolution of the Fgf and Fgfr gene families. Trends Genet. *20*, 563-569.

Leali, D., Alessi, P., Coltrini, D., Ronca, R., Corsini, M., Nardo, G., Indraccolo, S., and Presta, M. (2011). Long pentraxin-3 inhibits FGF8b-dependent angiogenesis and growth of steroid hormone-regulated tumors. Mol. Cancer Ther. *10*, 1600-1610.

Leali, D., Bianchi, R., Bugatti, A., Nicoli, S., Mitola, S., Ragona, L., Tomaselli, S., Gallo, G., Catello, S., Rivieccio, V., *et al*. (2010). Fibroblast growth factor 2-antagonist activity of a long-pentraxin 3-derived anti-angiogenic pentapeptide. J. Cell. Mol. Med. *14*, 2109-2121.

Leali, D., Inforzato, A., Ronca, R., Bianchi, R., Belleri, M., Coltrini, D., Di Salle, E., Sironi, M., Norata, G. D., Bottazzi, B., *et al*. (2012). Long pentraxin 3/tumor necrosis factor-stimulated gene-6 interaction: a biological rheostat for fibroblast growth factor 2-mediated angiogenesis. Arterioscler. Thromb. Vasc. Biol. *32*, 696-703.

Lieu, C., Heymach, J., Overman, M., Tran, H., and Kopetz, S. (2011). Beyond VEGF: inhibition of the fibroblast growth factor pathway and antiangiogenesis. Clin. Cancer Res. *17*, 6130-6139.

Maiolo, D., Mitola, S., Leali, D., Oliviero, G., Ravelli, C., Bugatti, A., Depero, L. E., Presta, M., and Bergese, P. (2012). Role of nanomechanics in canonical and noncanonical pro-angiogenic ligand/VEGF receptor-2 activation. J. Am. Chem. Soc. *134*, 14573-14579.

Martin, A., David, V., and Quarles, L.D. (2012). Regulation and function of the FGF23/klotho endocrine pathways. Physiol Rev. *92*, 131-155.

Pagano, K., Torella, R., Foglieni, C., Bugatti, A., Tomaselli, S., Zetta, L., Presta, M., Rusnati, M., Taraboletti, G., Colombo, G., and Ragona, L. (2012). Direct and allosteric inhibition of the FGF2/HSPGs/FGFR1 ternary complex formation by an antiangiogenic, thrombospondin-1-mimic small molecule. PloS One *7*, e36990.

Plotnikov, A. N., Schlessinger, J., Hubbard, S. R., and Mohammadi, M. (1999). Structural basis for FGF receptor dimerization and activation. Cell *98*, 641-650.

Polnaszek, N., Kwabi-Addo, B., Peterson, L. E., Ozen, M., Greenberg, N. M., Ortega, S., Basilico, C., and Ittmann, M. (2003). Fibroblast growth factor 2 promotes tumor progression in an autochthonous mouse model of prostate cancer. Cancer Res. *63*, 5754-5760.

Presta, M., Camozzi, M., Salvatori, G., and Rusnati, M. (2007). Role of the soluble pattern recognition receptor PTX3 in vascular biology. J. Cell. Mol. Med. *11*, 723-738.

Presta, M., Oreste, P., Zoppetti, G., Belleri, M., Tanghetti, E., Leali, D., Urbinati, C., Bugatti, A., Ronca, R., Nicoli, S., *et al*. (2005). Antiangiogenic activity of semisynthetic biotechnological heparins: low-molecular-weight-sulfated Escherichia coli K5 polysaccharide derivatives as fibroblast growth factor antagonists. Arterioscler. Thromb. Vasc. Biol. *25*, 71-76.

Richard, C., Liuzzo, J. P., and Moscatelli, D. (1995). Fibroblast growth factor-2 can mediate cell attachment by linking receptors and heparan sulfate proteoglycans on neighboring cells. J. Biol. Chem. *270*, 24188-24196.

Ronca, R., Alessi, P., Coltrini, D., Di Salle, E., Giacomini, A., Leali, D., Corsini, M., Belleri, M., Tobia, C., Garlanda, C., *et al*. (2013a). Long pentraxin-3 as an epithelial-stromal fibroblast growth factor-targeting inhibitor in prostate cancer. J. Pathol. *230*, 228-238.

Ronca, R., Di Salle, E., Giacomini, A., Leali, D., Alessi, P., Coltrini, D., Ravelli, C., Matarazzo, S., Ribatti, D., Vermi, W., and Presta, M. (2013b). Long Pentraxin-3 Inhibits Epithelial-Mesenchymal Transition in Melanoma Cells. Mol. Cancer Ther. *12*, 2760-2771.

Shojaei, F., Wu, X., Qu, X., Kowanetz, M., Yu, L., Tan, M., Meng, Y. G., and Ferrara, N. (2009). G-CSF-initiated myeloid cell mobilization and angiogenesis mediate tumor refractoriness to anti-VEGF therapy in mouse models. Proc. Natl. Acad. Sci. U S A *106*, 6742-6747.

Sun, H. D., Malabunga, M., Tonra, J. R., DiRenzo, R., Carrick, F. E., Zheng, H., Berthoud, H. R., McGuinness, O. P., Shen, J., Bohlen, P., *et al*. (2007). Monoclonal antibody antagonists of hypothalamic FGFR1 cause potent but reversible hypophagia and weight loss in rodents and monkeys. Am. J. Physiol. Endocrinol. Metab. *292*, E964-976.

Talmadge, J. E., and Hart, I. R. (1984). Inhibited growth of a reticulum cell sarcoma (M5076) induced in vitro and in vivo by macrophage-activating agents. Cancer Res. *44*, 2446-2451.

Urakawa, I., Yamazaki,Y., Shimada, T., Iijima, K., Hasegawa, H., Okawa, K., Fujita, T., Fukumoto, S., and Yamashita, T. (2006). Klotho converts canonical FGF receptor into a specific receptor for FGF23. Nature *444*, 770-774.

Zhang, X., Ibrahimi, O. A., Olsen, S. K., Umemori, H., Mohammadi, M., and Ornitz, D. M. (2006). Receptor specificity of the fibroblast growth factor family. The complete mammalian FGF family. J. Biol. Chem. *281*, 15694-15700.

FIGURE LEGENDS

Figure 1. Transgenic TgN(Tie2-hPTX3) mice.

A) RT-PCR and Western blot analyses of the expression of transgenic *hPTX3* in wild-type (WT) and TgN(Tie2-hPTX3) mice. **B)** Immunostaining of $CD31^+$ blood vessels (*red*) and hPTX3 protein (*green*). **C)** pFGFR1 (*red*) and CD31 (*green*) immunostaining of FGF2-stimulated endothelial cells isolated from WT and TgN(Tie2-hPTX3) lungs. Intensity of pFGFR1 signal was quantified and normalized to DAPI area. *Inset*: RT-PCR analysis on isolated cells. **D)** Fibrin-embedded aorta rings from WT and TgN(Tie2-hPTX3) mice treated with FGF2 or VEGF-A. Graph shows the number of sprouts at day 6. **E)** RT-qPCR (8 mice/group) and immunofluorescence analyses of *CD31* expression in vehicle and FGF2 Matrigel plugs (CD31 in *red*, hPTX3 in *green*). Scale bars: 50 μm (B, E), 30 μm (C), 400 μm (D). Data are mean ± SEM. * $P < 0.05$, # $P < 0.001$. See also Figure S1.

Figure 2. Transgenic *hPTX3* expression impairs heterotopic tumor growth.

A-C) TRAMP-C2/alginate plugs implanted in wild-type (WT) and TgN(Tie2-hPTX3) mice (8-10 mice/group). **A)** FGFR1 and pFGFR1 immunostaining and pFGFR1/FGFR quantification normalized to DAPI area. **B)** Western Blot analysis and pFGFR1/FGFR1 quantification normalized to β-actin. **C)** PTX3, CD31 and Ki67 immunostaining, $CD31^+$ and $Ki67^+$ quantification normalized to DAPI area and relative levels of *CD31* and *cyclin D1* mRNA expression normalized to *18S* rRNA. **D)** Growth of s.c. TRAMP-C2, LLC and B16-F10 tumors in WT and TgN(Tie2-hPTX3) mice (10-12 mice/group). **E)** Growth of s.c. TRAMP-C2 tumors in WT chimeric mice reconstituted with TgN(Tie2-hPTX3) or control TgN(Tie2-GFP) bone marrow (BM) (10 mice/group). M5076 (**F-G**) and B16-F10 (**H-I**) cells were injected i.v. in WT and TgN(Tie2-hPTX3) mice (10 mice/group). After 3 weeks, liver **(F)** and lungs **(H)** were weighted and macroscopic metastases were counted. Liver **(G)** and lungs **(I)** were H&E stained, double-immunostained for CD31 (*blue*)/PTX3 (*brown*) and immunostained for Ki67. Scale bars: 30 μm (A), 100 μm [B, G (CD31/PTX3 and Ki67), I (Ki67)], 200 μm [I (CD31/PTX3)], 400 μm [G, I (H&E)]. Data are mean ± SEM. * $P < 0.05$, ** $P < 0.01$, # $P < 0.001$. See also Figures S2, S3.

Figure 3. Transgenic *hPTX3* expression impairs orthotopic and multistage tumor growth.

A) Imaging of prostate Panc02-*luc* cells 9 and 20 days after orthotopic injection in WT and TgN(Tie2-hPTX3) mice (*top panel)* and Kaplan-Meyer survival curves (8-10 mice/group) (*bottom panel)*. **B)** Tumor growth, harvested tumors (*top panel)* and Kaplan-Meyer survival curves (*bottom panel)* for

EO771 mammary carcinoma grafts (10 mice/group). **C)** Histopathological analysis of anterior prostate lobes from 10 and 12 week-old TRAMP and TRAMP/Tie2-hPTX3 mice (8-12 mice/group). *Left graph* shows the percentage of pathologic area on total prostatic area; *right graph* shows the percentage of pathologic glands with well-differentiated (WD) carcinoma areas. Each dot represents a single tissue field and lines indicate the median values. **D)** Representative images of anterior prostate sections. **E-G)** $Ptx3^{-/-}$ *versus* WT and Tie2-hPTX3 mice. **E**) RT-qPCR analysis of *CD31* expression in PBS and FGF2 Matrigel plugs. **F)** Growth of s.c. B16-F10 tumors (10 mice/group)**. G)** Quantification of B16-F10 end-stage lung metastatic foci. Scale bar: 100 μm (D). Data are mean ± SEM. * $P < 0.05$, ** $P < 0.01$, # $P < 0.001$, ns = not significant.

Figure 4. NSC12 as a small molecule PTX3-derived FGF-trap.

A) Schematic representation of multimeric PTX3 protein, highlighting the N-terminal FGF-binding region ARPCA, and chemical structure of NSC12. **B)** Inhibition of HSPG/FGF2/FGFR1 ternary complex formation by NSC12. **C)** SPR competition assay for FGF2 binding to FGFR1 and heparin sensor chips in the presence of 100 μM NSC12 or NSC21. **D)** SPR and CONAMORE analysis of NSC12 affinity/binding on FGF2 sensor chip. **E)** Representation of the main binding mode of NSC12 predicted by docking and MD simulation of NSC12/FGF2 complex. NSC12 and the FGF2 side-chains in contact with NSC12 are shown as blue and cyan sticks, respectively, whereas FGF2 and FGFR (PDB id: 1fq9) are shown as yellow and gray cartoon, respectively. Magenta spheres refer to FGF2 residues involved in ARPCA interactions as deduced by MD simulations. **F)** Affinity (K_d) of NSC12/FGF interactions assessed by SPR. **G)** NSC12 inhibits HSPG/FGF/FGFR1 ternary complex formation by FGFR1(IIIc)-binding FGFs and **(H)** MMT-assessed KATO III cell proliferation triggered by FGFR2(IIIb)-binding FGFs. Data are mean ± SEM. NS, not stimulated. * $P < 0.05$, ** $P < 0.01$, # $P < 0.001$. See also Figures S4.

Figure 5. In vitro anti-tumor effects of NSC12.

A-B) FGFR1 (*green*) and pFGFR1 (*red*) immunostaining (**A**), viable cell counting and cell cycle analysis (**B**) of HUVE cells treated with FGF2, VEGF-A or FBS in the presence of NSC12 or NSC21. **C)** HUVE cell spheroids were stimulated with FGF2 or VEGF-A in the absence or presence of 1.0 μM NSC12 or NSC21. After 24 hours the number of sprouts/spheroid were counted. **D)** FGF2 and VEGF-A alginate pellets were placed on top of the chick embryo CAM at day 11 in the absence or presence of NSC12 or NSC21. At day 14 blood vessels around the sponges were counted (8 eggs/group). **E-F)**

Viable cell counting and cell cycle analysis of murine (TRAMP-C2) and human (LNCaP, DU145) prostate cancer cells (**E**) and of murine (LLC) and human (H520, HCC827) lung cancer cells (**F**). * $P < 0.05$, # $P < 0.001$. Scale bars: 20 μm (A), 100 μm (C). Data are mean ± SEM. For cell cycle analyses: $P < 0.01$, *S phase, °G0/G1 phase, §G2/M phase. See also Figure S5.

Figure 6. NSC12 inhibits the FGF/FGFR system in FGF-dependent tumors.

A-D) Male mice were implanted s.c. with TRAMP-C2/alginate plugs and treated i.p. every other day with NSC12, NSC21 or vehicle (4-6 mice/group). After one week, harvested plugs were weighted (**A**) and processed for FGFR1/pFGFR1 (**B**) and CD31, Ki67 immunofluorescence analysis (**C**). **D)** pFGFR1/FGFR1 quantification by WB analysis of TRAMP-C2 plugs (data are normalized to β-actin). **E-G**) Mice implanted s.c with alginate plugs containing FGF-dependent human DU145 (**E**) or H520 (**F**) cells or FGF-independent human HCC827 (**G**) cells were treated i.p. every other day with 7.5 mg/Kg NSC12, NSC21 or vehicle for one week (4-6 mice/group). Harvested plugs were weighted and immunofluorescence analysis was performed. Scale bars: 30 μm (B), 50 μm [E, F, G (H&E)], 100 μm [E, F, G (CD31, TUNEL)]. Data are mean ± SEM. ** $P < 0.01$, # $P < 0.001$, § $P < 0.05$ *vs* NSC12 at 2.5 and 5 mg/Kg. See also Figure S6.

Figure 7. Anti-tumor and anti-metastatic activity of NSC12.

A) Growth of s.c. TRAMP-C2, DU145 and H520 tumors in mice treated i.p. (*arrows*) with NSC12, NSC21 or vehicle (10-16 mice/group). **B**) B16-F10-*luc* cells were injected i.v. and mice treated i.p for two weeks every other day with NSC12, NSC21 or vehicle (6-8 mice/group). Bioluminescence imaging of lung colonization at day 21 and count of lung macrometastases at day 28. **C**) Number of spontaneous lung macrometastases 5 weeks after primary EO771 tumor removal and treatment with DMSO, NSC12 or NSC21 (8-10 mice/group). **D)** Inhibition of FGFR1 activation in s.c. TRAMP-C2/alginate plugs after 4 day-oral treatment with NSC12 (7.5 mg/Kg, 4-6 mice/group). pFGFR1/FGFR1 was quantified and normalized to DAPI area. **E)** Growth of H520 tumors in mice orally treated (*arrows*) with NSC12, NSC21 or vehicle. At the end of the experiment, harvested tumors were photographed and weighted (10-12 mice/group). Scale bar: 30 μm. Data are mean ± SEM. * $P < 0.05$, ** $P < 0.01$, # $P < 0.001$, ns = not significant. See also Figure S7.

SUPPLEMENTAL INFORMATION

Supplemental Information includes 7 Supplemental Figures, 1 Supplemental Table, Supplemental Experimental Procedures and Supplemental References and can be found with this article online.

Figure 1
Click here to download Figure: Figure_1 64.tif

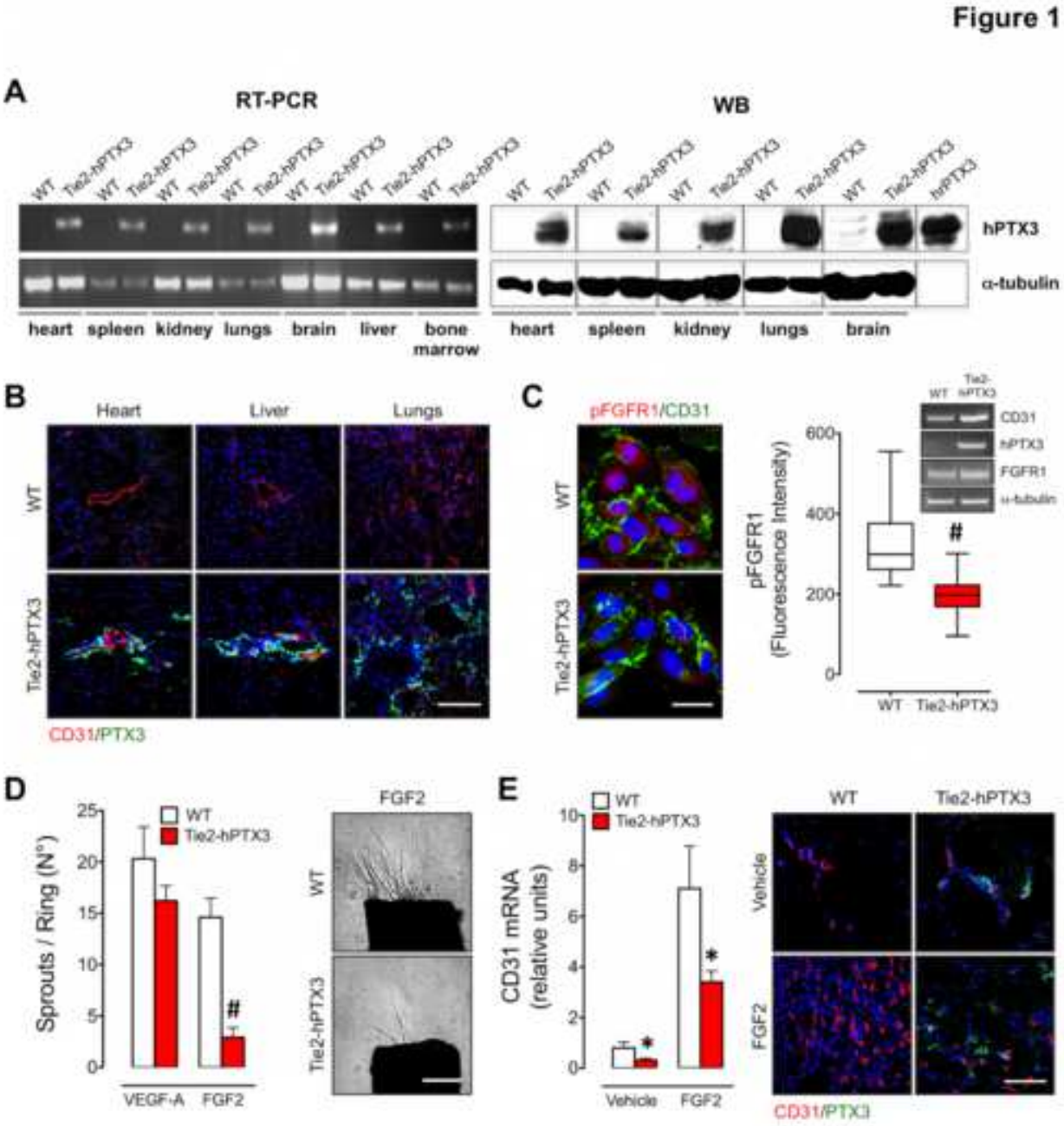

Figure 2

Click here to download Figure: Figure_2 64.tif

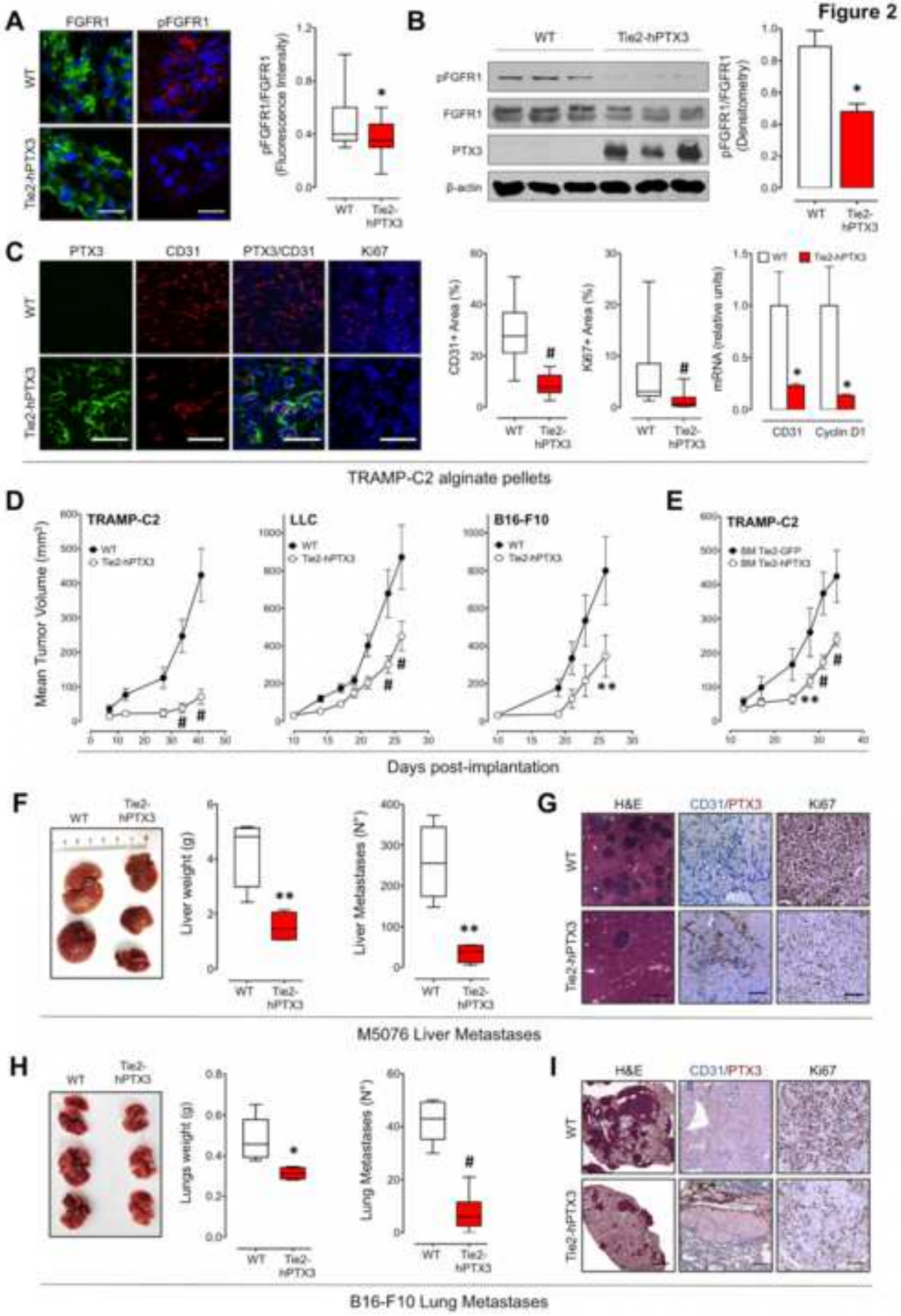

Figure 3

Click here to download Figure: Figure_3 64.tif

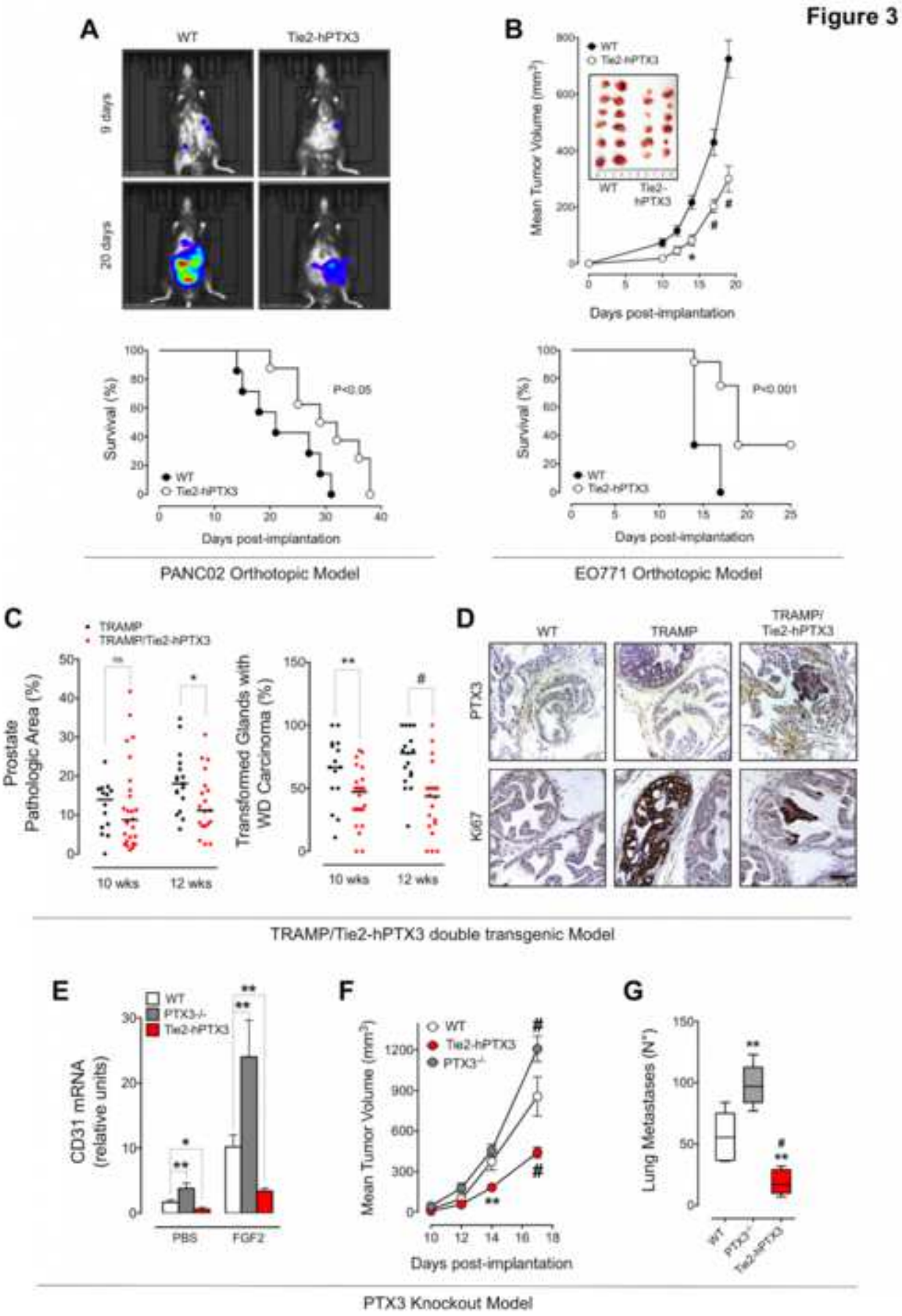

Figure 4

Click here to download Figure: Figure_4new 64.tiff

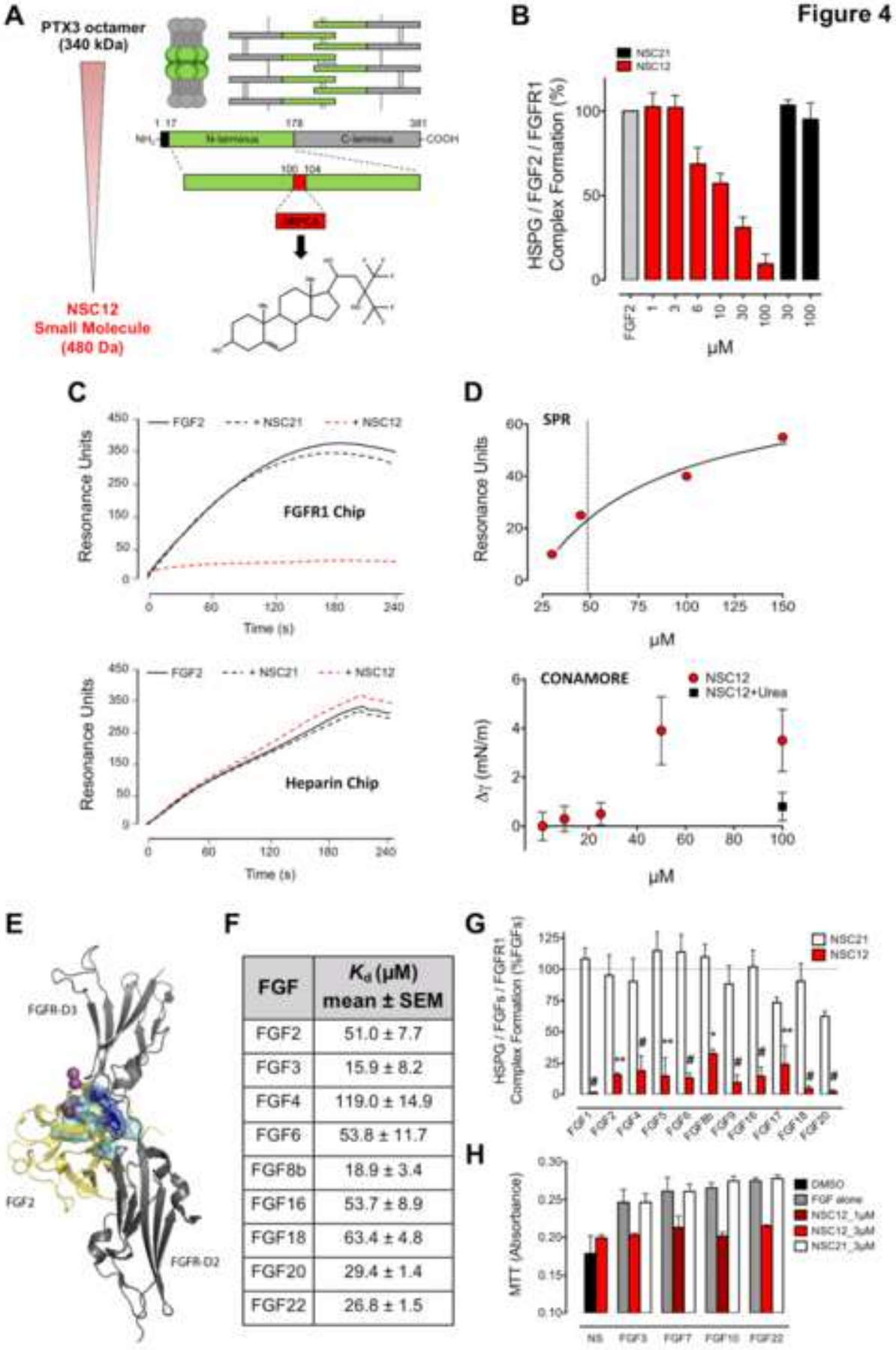

FGF	K_d (μM) mean ± SEM
FGF2	51.0 ± 7.7
FGF3	15.9 ± 8.2
FGF4	119.0 ± 14.9
FGF6	53.8 ± 11.7
FGF8b	18.9 ± 3.4
FGF16	53.7 ± 8.9
FGF18	63.4 ± 4.8
FGF20	29.4 ± 1.4
FGF22	26.8 ± 1.5

Figure 5

Click here to download Figure: Figure_5 64.tif

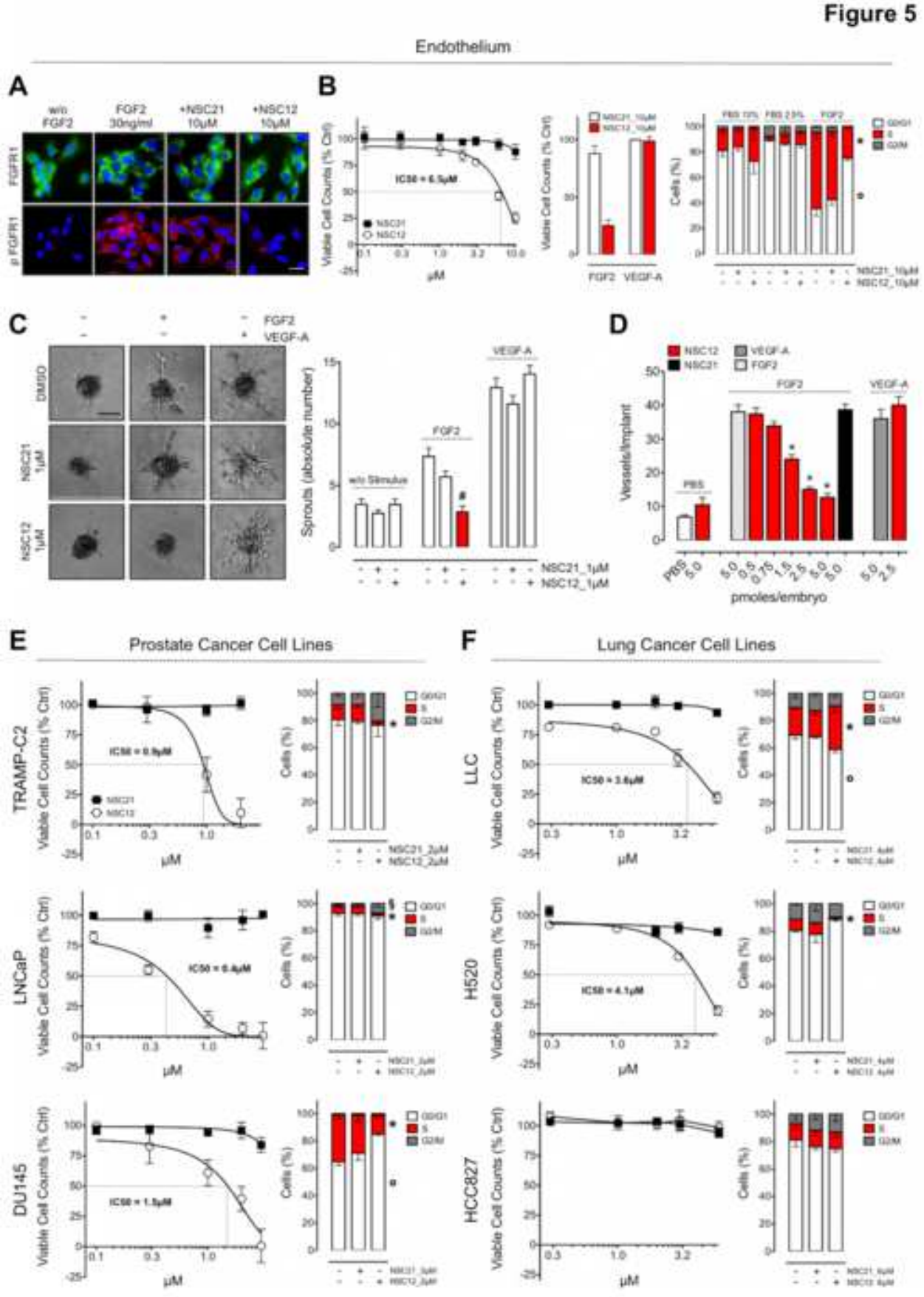

Figure 6

Click here to download Figure: Figure_6 64.tif

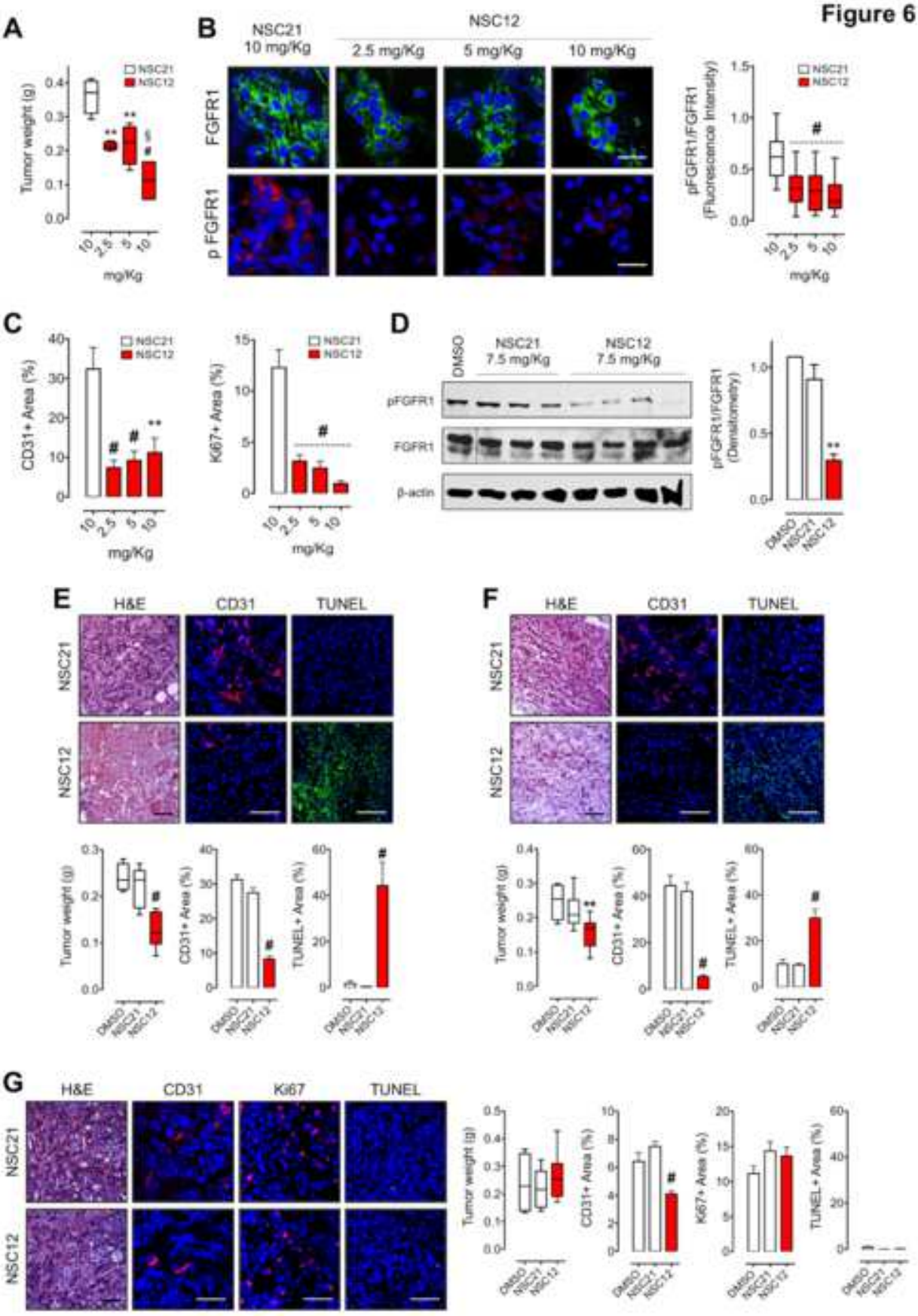

Figure 7

Click here to download Figure: Figure_7 64.tif

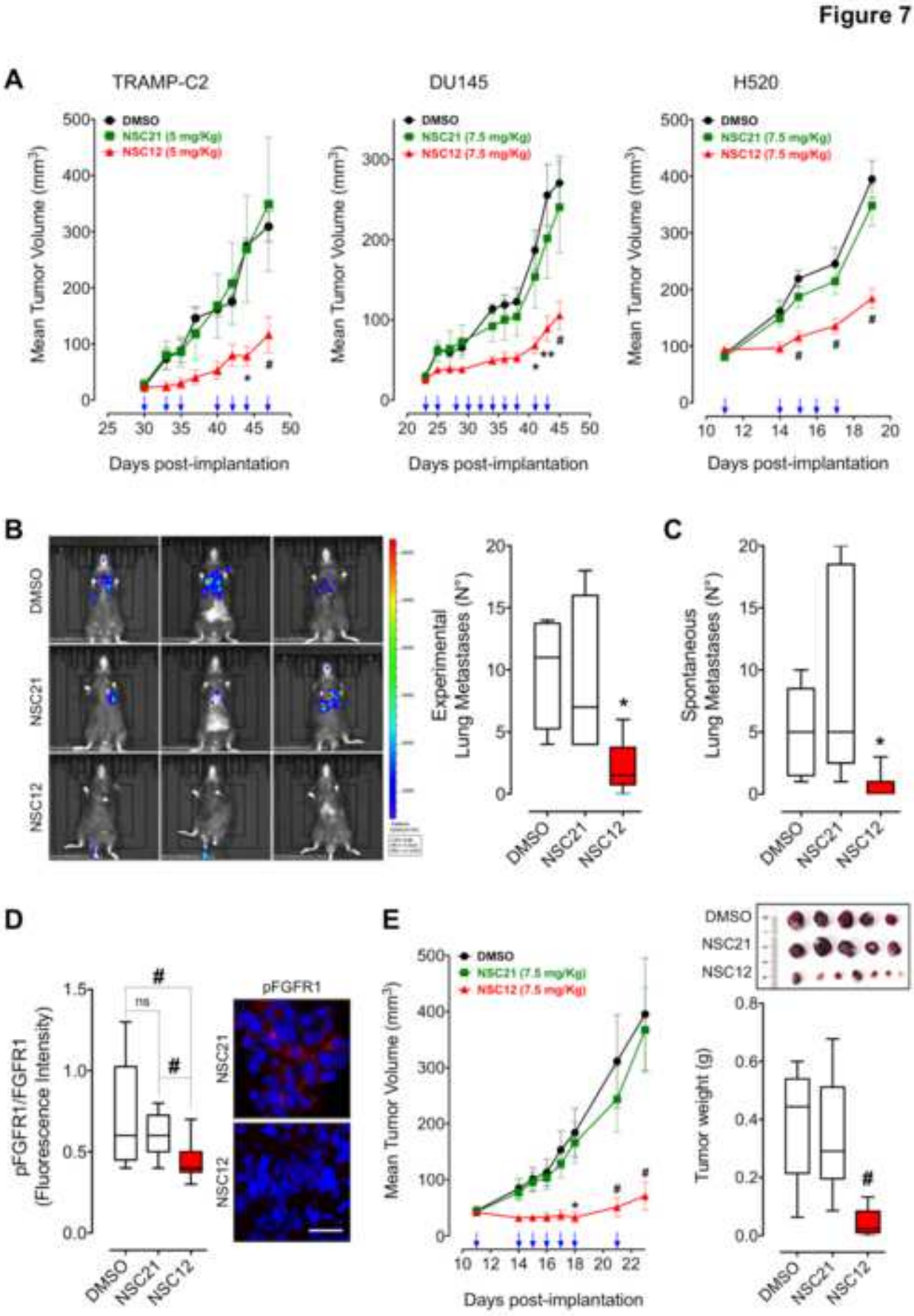

SUPPLEMENTAL INFORMATION

Supplemental Information includes Supplemental Figures S1-S7, Supplemental Table S1, Supplemental Experimental Procedures and Supplemental References.

SUPPLEMENTAL INFORMATION

SUPPLEMENTAL DATA

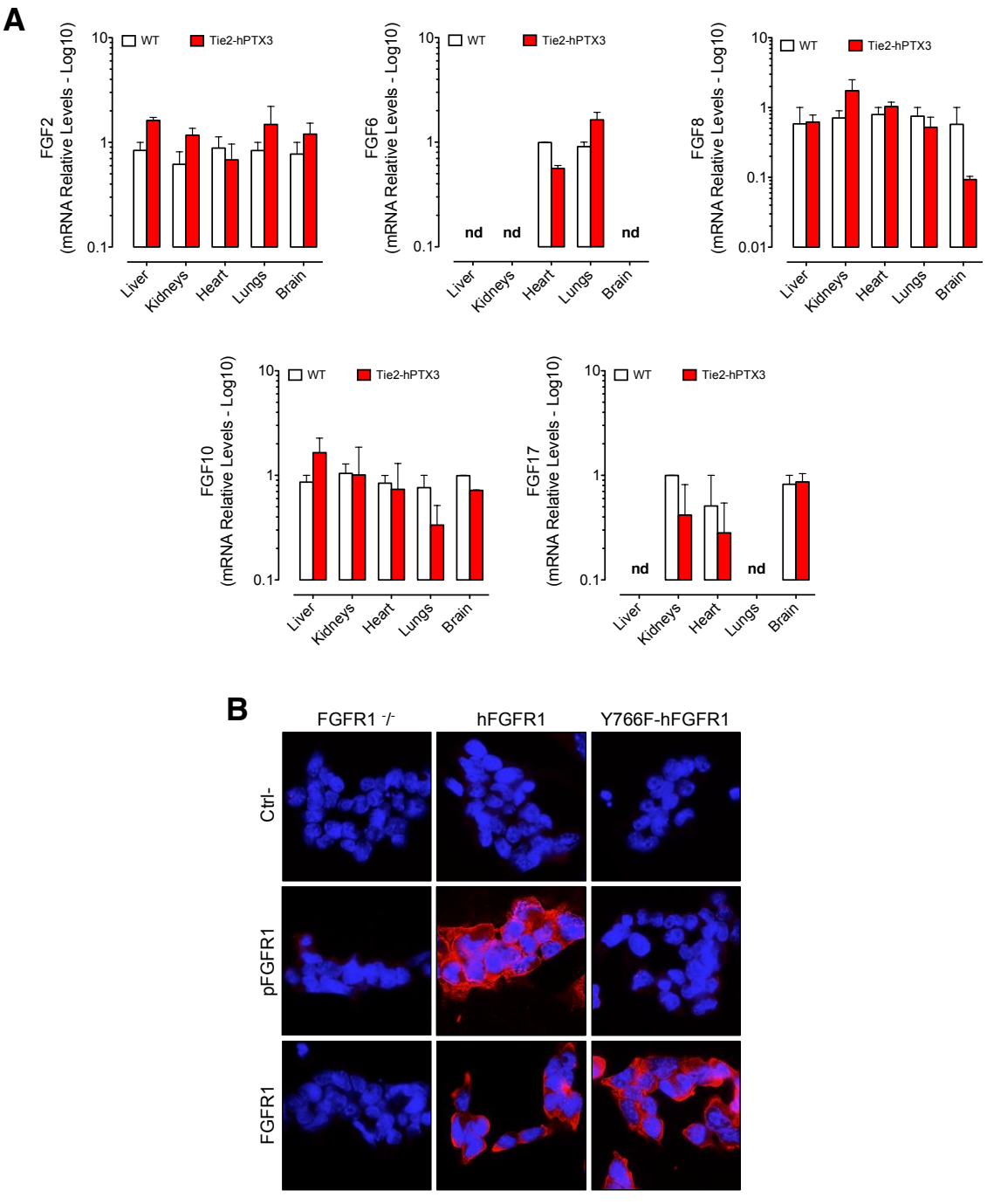

Figure S1, Related to Figure 1. FGF mRNA levels in wild type and TgN(Tie2-hPTX3) mice and specificity of FGFR1/pFGFR1 immunostaining.

A) The expression levels of PTX3-targeted FGFs [*i.e.* FGF2, FGF6, FGF8, FGF10 and FGF17; see (Ronca et al., 2013a)] was assessed on different organs of wild type (WT, white columns) and Tie2-

hPTX3 (red columns) mice by RT-qPCR analysis. For each organ, FGF expression levels were normalized to *Gapdh* expression and referred to those measured in one WT animal. Data are the mean ± SEM of 3 animals per group. nd = not detectable.

B) FGFR1-/- murine embryonic stem (ES) cells stably transfected with human FGFR1 (hFGFR1) or with the Y766F-hFGFR1 mutant cDNAs (Dell'Era at al., 2003) were stimulated with 30 ng/ml of FGF2 for 30 minutes and immunostained with anti-pFGFR1(Tyr766) and anti-FGFR1 antibodies (in red). As shown in the figure, the anti-FGFR1 antibody recognizes both transfectants but not FGFR1-/- ES cells whereas the anti-pFGFR1(Tyr766) antibody recognizes hFGFR1 transfectants but not FGFR1-/- ES cells nor the Y766F-hFGFR1 mutants. Ctrl-: omission of the primary antibody.

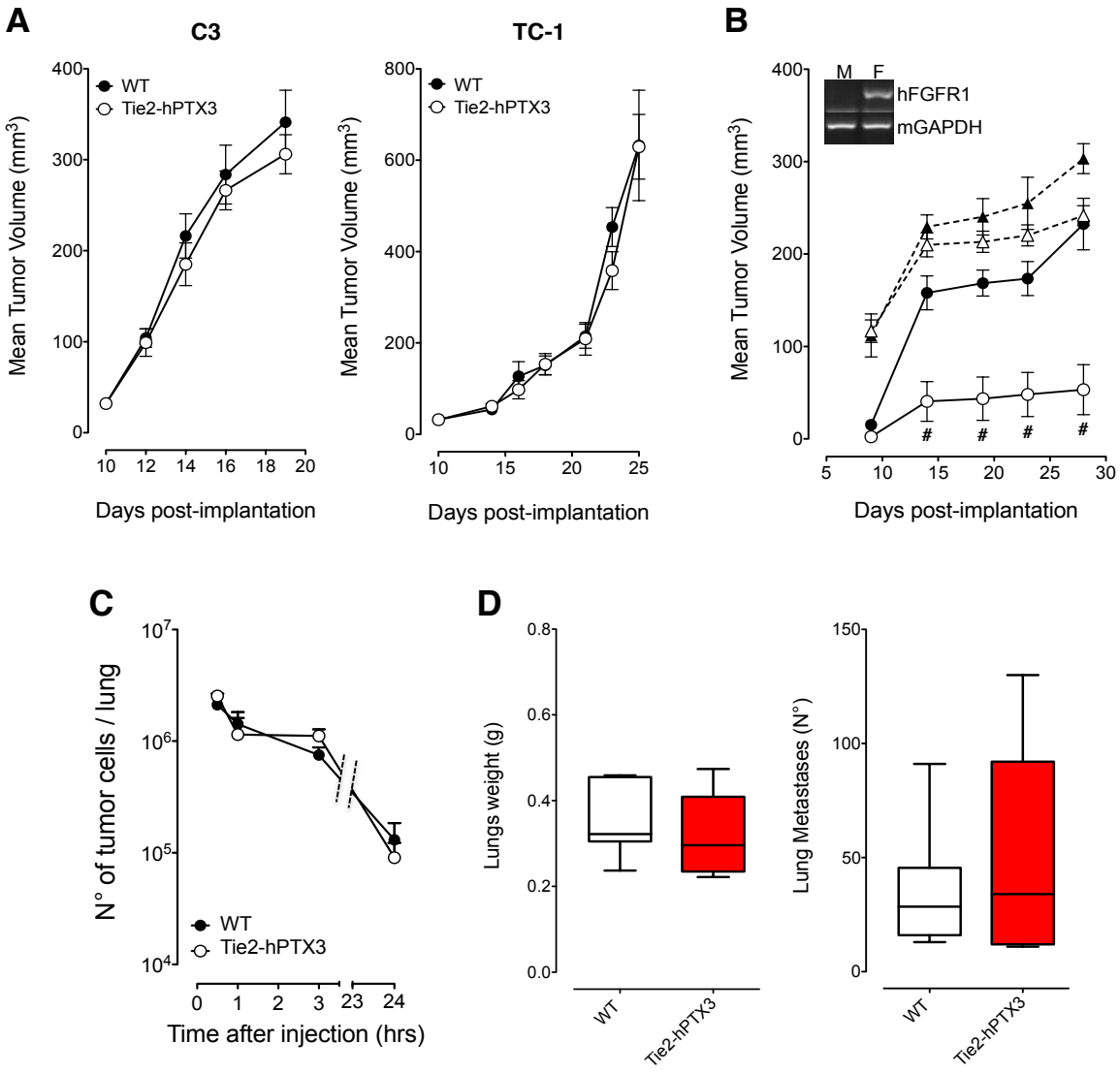

Figure S2, Related to Figure 2. *Tie2* promoter-driven hPTX3 expression in transgenic mice does not affect the tumorigenic potential of FGF/FGFR-independent tumor cells, the homing of B16-F10 cells to the lungs of transgenic mice and the metastatic potential of FGF/FGFR-independent tumor cells.

A) C3 and TC-1 were injected s.c. in wild-type (●) and TgN(Tie2-hPTX3) mice (○).
B) TRAMP-C2 (● and ○) and hFGFR1-TRAMP-C2 (▲ and Δ) cells (the latter ones overexpressing a constitutively activated form of the intracellular TK domain of human FGFR1) were injected s.c. in wild-type (*black symbols*) and TgN(Tie2-hPTX3) mice (*white symbols*). ▲= hFGFR1-TRAMP-C2 cells in WT mice, Δ= hFGFR1-TRAMP-C2 cells in Tie2-hPTX3 mice, ●= TRAMP-C2 in WT mice, ○= TRAMP-C2 in Tie2-hPTX3 mice. *Inset*: semiquantitative RT-PCR analysis of hFGFR1-TRAMP-C2 cells confirms the expression of the constitutively activated form of the receptor (M = control/untransfected cells, F = hFGFR1 transfected cells). Tumor growth was measured with calliper (mean ± SEM, 10 mice/group); # $p<0.001$.
C) B16-F10 cells stably transfected with an empty pBABE vector were injected at 6.6 x 10^5 cells/mouse into the tail vein of wild-type (●) and TgN(Tie2-hPTX3) mice (○). Animals were sacrificed at 0.5, 1, 3

and 24 hours after injection, genomic DNA was extracted from harvested lungs and the number of homing B16-F10 cells was measured by quantitative PCR of the *psi* (Ψ) encapsidation sequence of the pBABE plasmid backbone. The absolute number of injected cells present in the lungs was calculated by linear interpolation of the obtained DDCt values with the values of a standard curve generated by mixing not injected lung tissue with an increasing number of pBABE-transfected B16-F10 cells. Data are the mean ± SEM; 10 mice/group.

D) TC-1 cells were injected i.v. in wild-type and TgN(Tie2-hPTX3) mice (10 mice/group). After 3 weeks lungs were harvested, weighted and metastatic foci were counted under a dissecting microscope. The boxes extend from the 25th to the 75th percentiles, the lines indicate the median values, and the whiskers indicate the range of values.

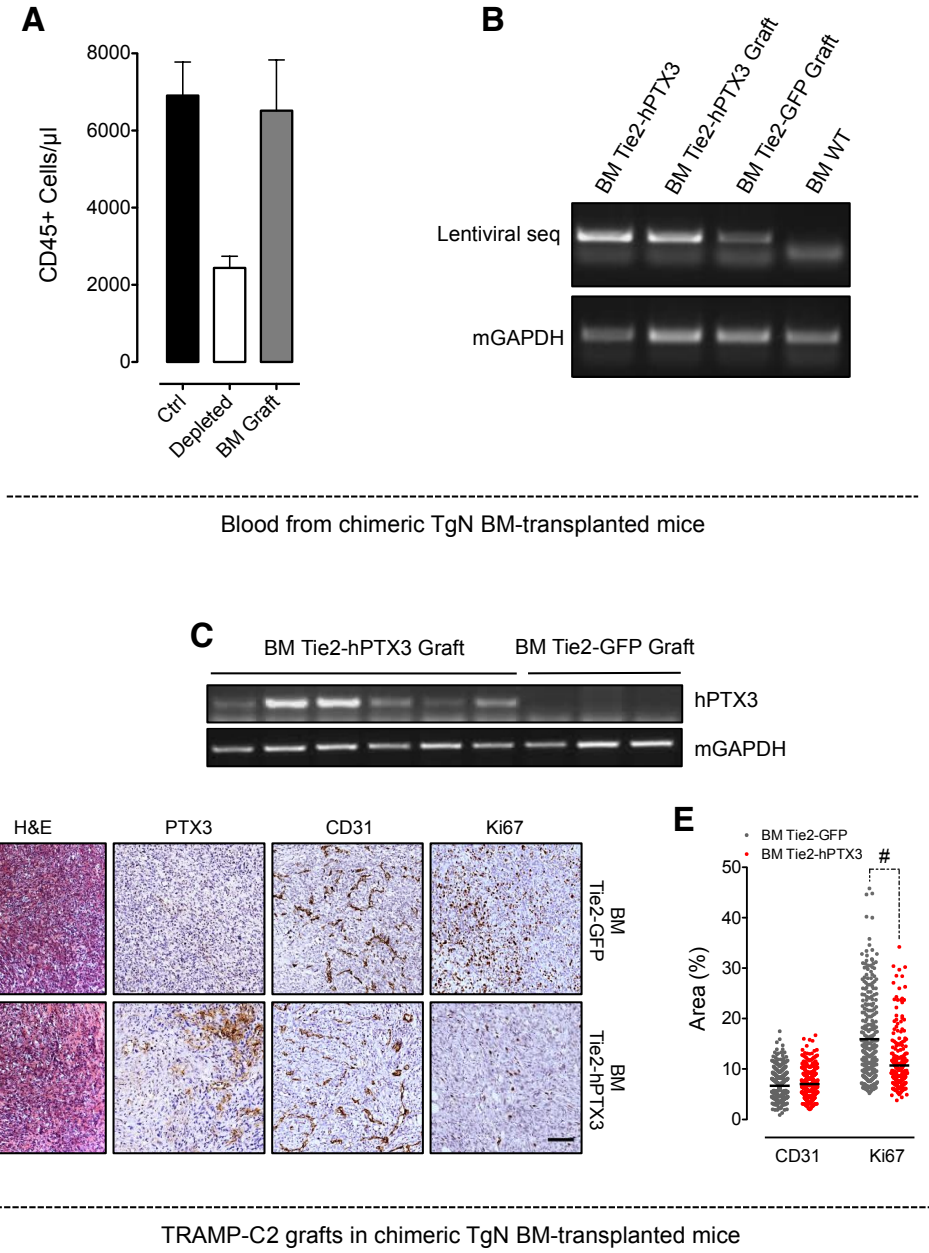

Figure S3, Related to Figure 2. Analysis of chimeric TgN(Tie2-hPTX3) bone marrow-transplanted mice.

A) Cytofluorimetric analysis of peripheral blood $CD45^+$ cells in immunodepleted wild-type mice 4 weeks after TgN(Tie2-hPTX3) bone marrow transplantation (BM Graft) compared with mice before (Ctrl) and 4 days after busulfan myelodepletion (Depleted).
B) PCR analysis of the genomic DNA from the peripheral blood of wild-type mice reconstituted with TgN(Tie2-hPTX3) or TgN(Tie2-GFP) BM grafts. Lentiviral sequences allow the detection of blood cells derived from the BM of lentivirus-generated transgenic mice. The BM from TgN(Tie2-hPTX3) and wild-type mice were used as positive and negative controls, respectively.
C) RT-PCR analysis for the detection of *Tie2* promoter-driven expression by TEMs of *hPTX3* mRNA in s.c. TRAMP-C2 tumors harvested from myelodepleted wild-type mice reconstituted with TgN(Tie2-hPTX3) or TgN(Tie2-GFP) BM.

D) TRAMP-C2 tumors explanted from TgN(Tie2-hPTX3) or TgN(Tie2-GFP) BM-transplanted mice were H&E stained and immunostained for PTX3, CD31 and Ki67.
E) The graph shows the quantification of $CD31^+$ and $Ki67^+$ immunoreactive areas. Each dot represents the value obtained from the analysis of a single tissue field and the lines indicate the mean values. Scale bar: 50 μm; # $p<0.001$.

A

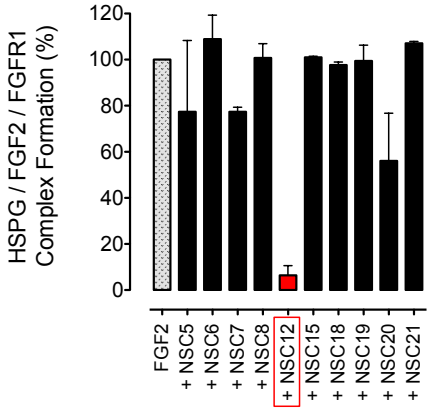

Current name	NCI/NSC code	Chemical name
NSC5	NSC105539	2-ethyl-2-hydroxy-N-phenylbutanamide
NSC6	NSC120340	1,1'-(4-methylbenzene-1,3-diyl)bis[3-(2-chloroethyl)urea]
NSC7	NSC131257	(4Z)-N-[(E)-(2-chlorophenyl)methylideneamino]-4-(dimethylaminohydrazinylidene)-5-methylpyrazole-3-carboxamide
NSC8	NSC142655	1-(4-methylphenyl)sulfonyl-3-(3-propan-2-yloxypropyl)urea
NSC12	NSC172285	4,4,4-trifluoro-1-(3-hydroxy-10,13-dimethyl-2,3,4,7,8,9,11,12,14,15,16,17-dodecahydro-1H-cyclopenta[a]phenanthren-17-yl)-3-(trifluoromethyl)butane-1,3-diol
NSC15	NSC205553	1-(2-chlorophenyl)-3-[(E)-4-methylpentan-2-ylideneamino]urea
NSC18	NSC328907	5-amino-1-methyl-1,2,3,4,9,10-hexahydroanthracene-9,10-diol
NSC19	NSC377849	1-(diethylamino)-3-(2,6-diethylphenyl)urea
NSC20	NSC400267	1-[butyl(ethyl)amino]-3-phenylthiourea
NSC21	NSC601853	methyl N-[6,7,8-trimethoxy-2-(methoxycarbonylamino)-4-oxo-1,3-dihydroquinazolin-2-yl]carbamate

B

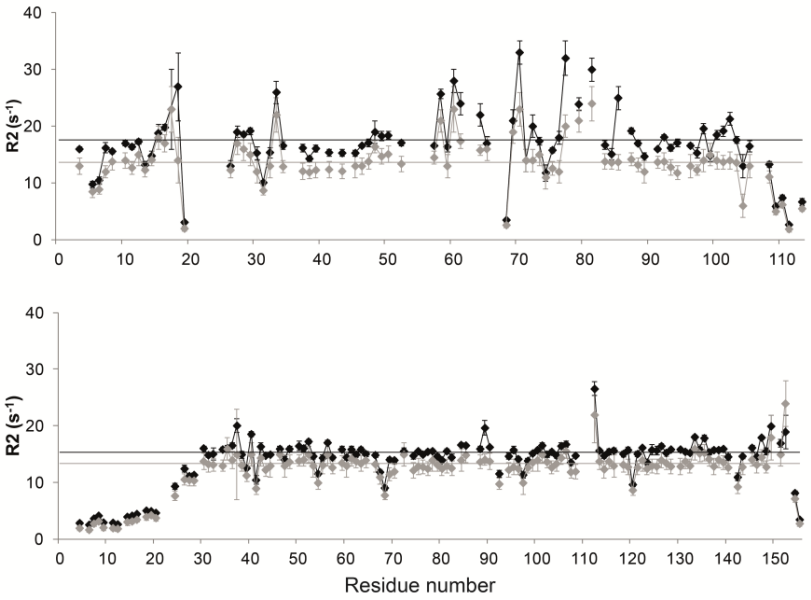

C

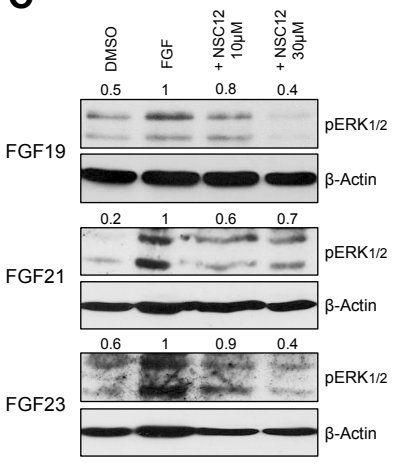

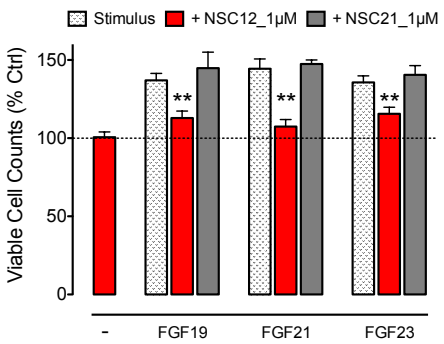

D

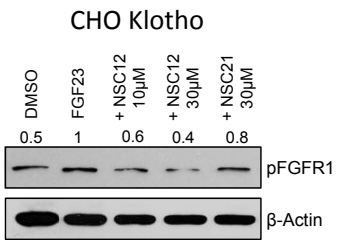

Figure S4, Related to Figure 4. Preliminary screening of candidate PTX3-derived small molecules, NMR analysis of NSC12 effects on FGF2/D2 complex, and NSC12 activity on hormonal FGFs.

A) ***Left graph*** represents the preliminary screening performed with different candidate compounds obtained from Drug Synthesis and Chemistry Branch, Developmental Therapeutics Program, Division of Cancer Treatment and Diagnosis, National Cancer Institute (NCI). These molecules were tested at the concentration of 100 μM for their capacity to inhibit the formation of the HSPG/FGF2/FGFR1 ternary complex in a HSPG/FGF2/FGFR1 mediated cell-cell adhesion assay. Data, expressed as the percentage of cells bound in the absence of any competitor, were performed in triplicate and are the mean ± SEM. NSC12 appeared as the most active compound whereas NSC21 was fully inactive. ***Right panel*** shows the name assigned to the compounds tested (current name), their original NCI/NSC code and chemical name.

B) ^{15}N transverse relaxation rate values (R2) of D2 (upper panel) and FGF2 (lower panel) as a function of the residue number are reported for FGF2/D2 complex, in the absence (black symbols) and in the presence (grey symbols) of NSC12. The horizontal black and grey lines represent the average R2 values in the absence and in the presence of NSC12, respectively.

C) ***Left panel.*** MDA-MB-361 cells were stimulated with FGF19, FGF21 or FGF23 (100 ng/ml) in the absence or presence of 10 μM or 30 μM NSC12. After 20 minutes of incubation, $ERK_{1/2}$ phosphorylation was assessed by Western blotting. Densitometry values were normalized for β-actin levels and expressed as ratio over FGF**.** ***Right panel.*** MDA-MB-361 cells were seeded in low serum (1% FBS) and stimulated with recombinant FGF19, FGF21 or FGF23 (all at 30 ng/ml) as described (Roidl et al., 2010) in the absence or in the presence of NSC12 or NSC21 (both at 1 μM). 72 hours after treatment, viable cells were counted by the counting function of the MACSQuant Analyzer (Miltenyi Biotec) and data expressed as percentage in respect to non-stimulated controls (% Ctrl). **, $P<0.01$.

D) CHO transfectants overexpressing αKlotho were stimulated with FGF23 (100 ng/ml) in the absence or presence of 10 μM or 30 μM NSC12 or 30 μM NSC21. After 20 minutes of incubation, FGFR1 phosphorylation was assessed by Western blotting with anti-pFGFR1(Tyr766) antibody. Densitometry values were normalized for β-actin levels and expressed as ratio over FGF23**.**

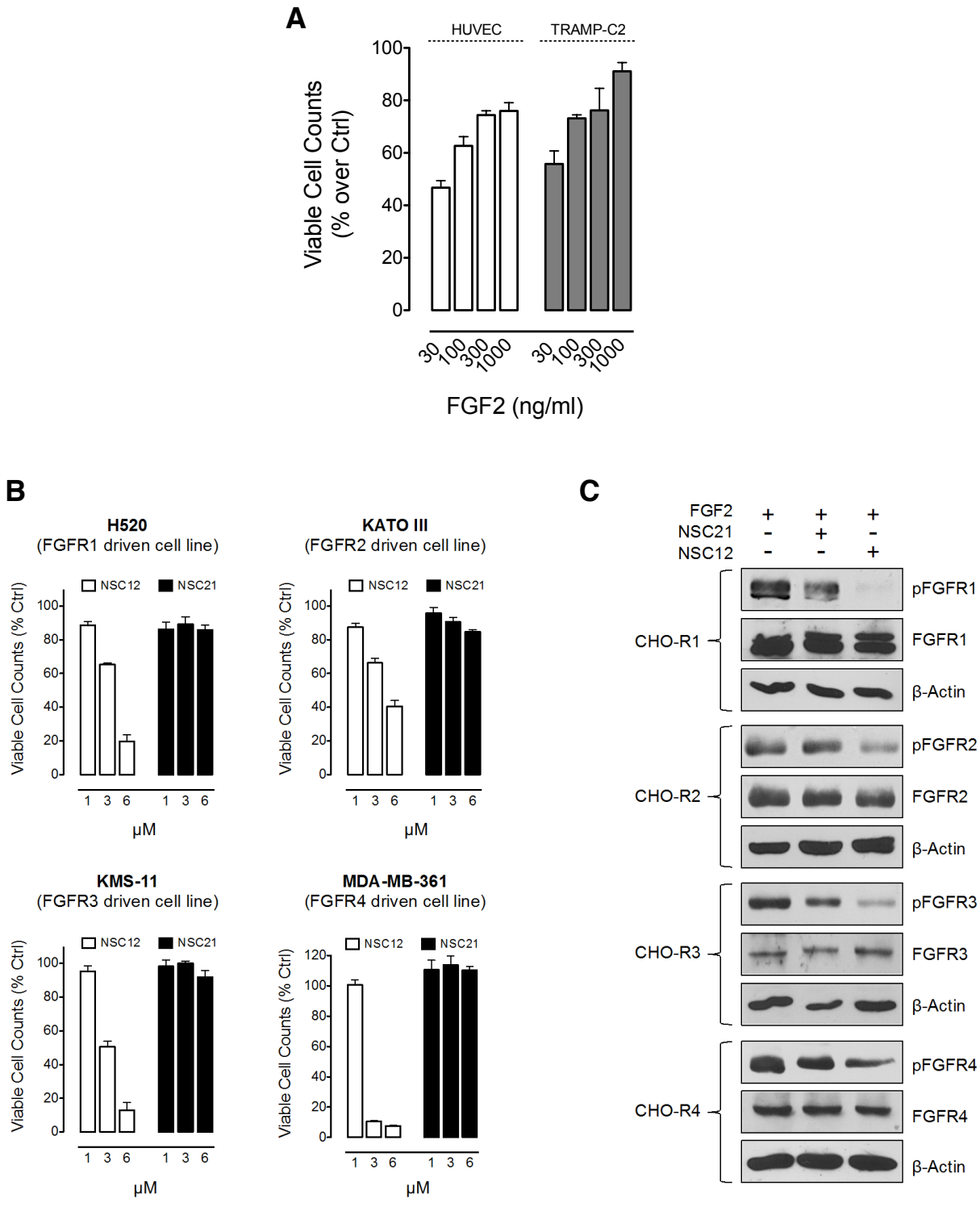

Figure S5, Related to Figure 5. The inhibitory effect of NSC12 is rescued by an excess of FGF2 and NSC12 impairs the proliferation of FGFR1-4-driven human tumor cells and FGFR1-4 phosphorylation.

A) HUVECs (white bars) and TRAMP-C2 cells (grey bars) where treated for 48 hours with NSC12 at the corresponding IC_{50} dose (6.5 μM and 1.0 μM, respectively) in the presence of increasing

concentrations of recombinant FGF2. Cells were counted at the end of incubation and data are expressed as the number of viable cells in respect to control untreated cells.
B) FGFR1-driven H520 cells (also shown in Figure 5F), FGFR2-driven KATO III cells, FGFR3-driven KMS-11 cells and FGFR4-driven MDA-MB-361 cells where treated with NSC12 or the control compound NSC21. After 48 hours, the number of viable cells was assessed and data are expressed as the number of viable cells in respect to control untreated cells.
C) CHO transfectants overexpressing FGFR1, FGFR2, FGFR3 or FGFR4 where stimulated with FGF2 (30 ng/ml) in the absence or presence of NSC12 or NSC21 (both at 30 μM). After 20 minutes of incubation, FGFR phosphorylation was assessed by Western blotting with anti-phosphotyrosine antibodies.

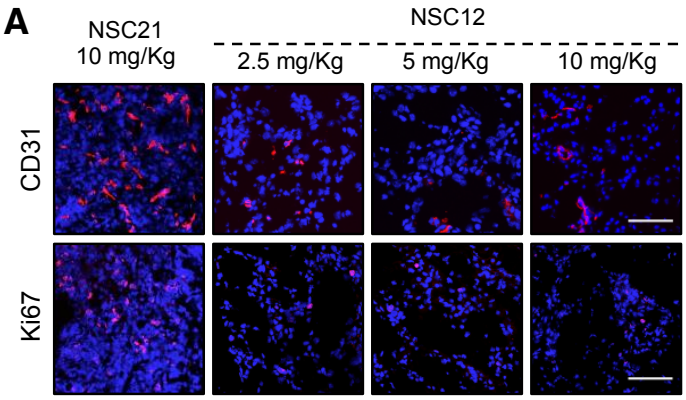

B

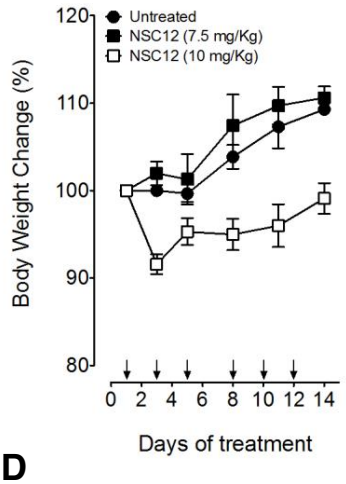

C

		Untreated mice	NSC12 treated mice
BLOOD PARAMETERS	White blood cells (10^3/µL)	7.0 ± 2.1	8.4 ± 1.4
	Neutrophils (%)	7.9 ± 2.4	9.2 ± 2.7
	Lymphocytes (%)	88.8 ± 1.7	86.1 ± 3.1
	Monocytes (%)	0.4 ± 0.3	0.4 ± 0.4
	Eosinophils (%)	0.8± 0.5	1.4 ± 0.7
	Basophils (%)	2.3 ± 0.4	2.9 ± 0.5
	Red blood cells (10^6/µL)	9.0 ± 1.7	10.3 ± 0.3
	Hemoglobin (g/dL)	14.7 ± 2.5	16.4 ± 0.7
	Hematocrit (%)	41.1 ± 6.8	46 ± 0.9
	Molecular Corpuscular Volume (fL)	45.9 ± 1.0	44.7 ± 0.4
	Molecular corpuscular Hemoglobin (pg)	16.4 ± 0.5	15.9 ± 0.2
	Mean Corpuscular Haemoglob Conc. (g/dL)	35.9 ± 0.4	35.6 ± 0.8
	RDW (%)	17.7 ± 0.7	20.9 ± 0.4
	Platelets (10^3/µL)	743.3 ± 125.5	633 ± 158.2
BIOCHEMICAL PARAMETERS	ALT (U/L)	36.5 ± 0.7	44.5 ± 4.1
	AST (U/L)	115.7 ± 43.1	160 ± 17.3
	Albumin/globulin (A/G) ratio	1.9 ± 0.3	1.8 ± 0.1
	CK (U/L)	438 ± 336.6	564.0 ± 290.6
	LDH (U/L)	1975 ± 483.5	2234.0 ± 339.3
	Urea (mmol/L)	7.5 ± 1.4	7.1 ± 0.5
	Albumin (g/L)	32.3 ± 3.8	35.2 ± 3.8
	Total proteins (g/L)	52.3 ± 2.3	58.2 ± 2.8
	Phosphorus (mmol/L)	2.2 ± 0.2	2.5 ± 0.2
	Calcium (mmol/L)	1.5 ± 0.2	2.0 ± 0.2
	Potassium (mmol/L)	7.0 ± 0.7	7.9 ± 0.4

D

Hormonal FGFs	Untreated (pg/ml)	NSC12 (pg/ml)
FGF19	< 2.9	< 2.9
FGF21	346.8 ± 34.3	264.8 ± 11.2
FGF23	30.0 ± 4.9	40.9 ± 13.6

Figure S6, Related to Figure 6. Immunostaining of TRAMP-C2 plugs, body weight variation and haematological parameters of mice after treatment with NSC12.

A) Male mice were implanted s.c. with alginate plugs containing TRAMP-C2 cells and treated i.p. every other day with NSC12, NSC21 or vehicle (4-6 mice/group). After one week, harvested plugs were processed for CD31 and Ki67 immunofluorescence analysis; scale bars: 100µm.
B) Body weight variation following treatment with NSC12 at 7.5 or 10 mg/kg. Mice were treated i.p. every other day (arrows) and weighted for two weeks. Body weight variation is shown in respect to time 0.
C) Blood components, biochemical serum parameters and **D)** circulating levels of hormonal FGFs (assessed by serum ELISA) were determined after two weeks of i.p. treatment with NSC12 at 7.5 mg/kg. Data are the mean ± SEM of 5 or more animals.

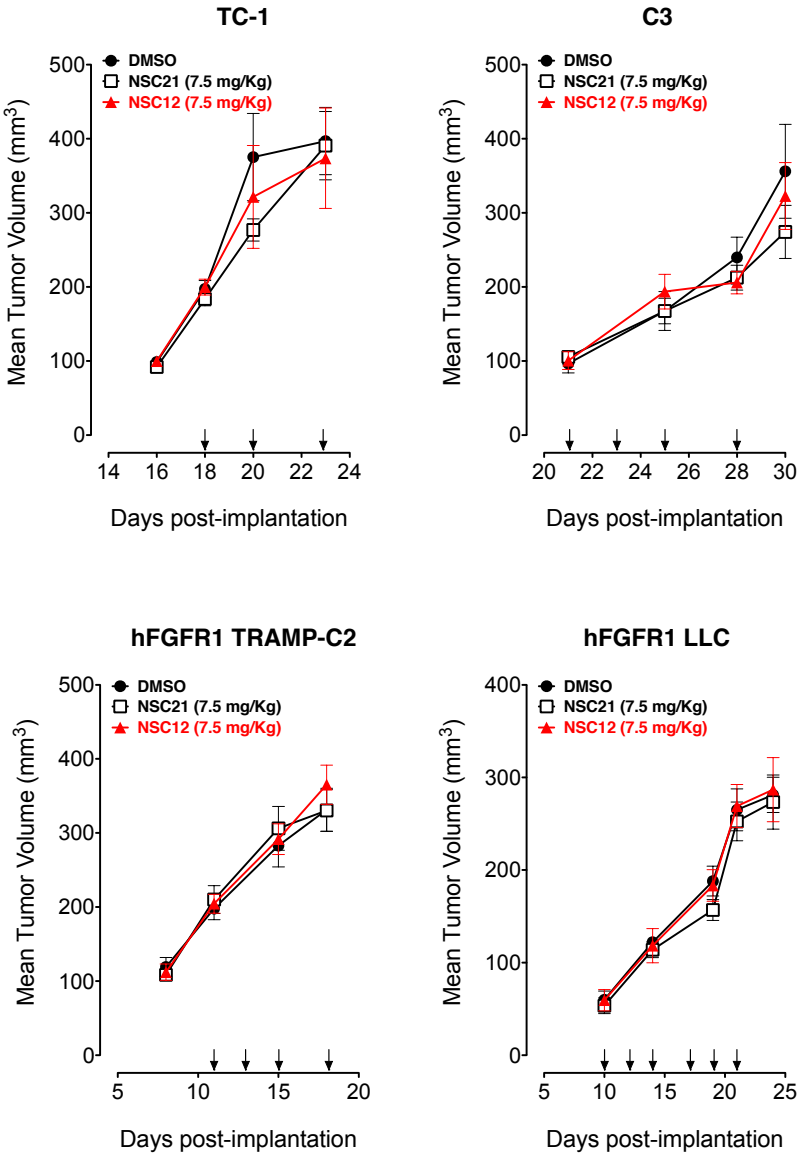

Figure S7, Related to Figure 7. Treatment with NSC12 does not affect the growth of FGF-independent tumors.

FGF-independent TC1 and C3 cells, and hFGFR1-TRAMP-C2 and hFGFR1-LLC cells, both harbouring a ligand-independent constitutively activated form of FGFR1, where grafted s.c. in the flanks of syngeneic animals. Tumor bearing mice were treated i.p. (arrows) with vehicle (DMSO), NSC12 or NSC21 at 7.5 mg/kg. Data are the mean ± SEM of 10 mice/group.

NSC12-targeted FGF	Related putative FGF-dependent human tumors	References
FGF1	Breast, pancreatic, prostate cancer	(Ghaneh et al., 2002; Penault-Llorca et al., 1995; Shain et al., 1996)
FGF2	Melanoma, bladder, prostate, breast, pancreatic, small cell lung cancer	(Berger et al., 1999; Penault-Llorca et al., 1995; Ronca et al., 2013b; Ruotsalainen et al., 2002; Yamanaka et al., 1993; Yoshimura et al., 1996)
FGF3	Bladder, mammary, gastric and non-small cell lung cancer	(Soria et al., 2014; Tai et al., 2006; Yoshida et al., 1988; Zaharieva et al., 2003)
FGF4	Lymphoma, hepatocellular carcinoma, ovarian, breast cancer	(Arao et al., 2013; Cao et al., 2014; Soria et al., 2014; Yasuda et al., 2014; Zaharieva et al., 2003)
FGF5	Glioblastoma multiforme, melanoma, bladder, pancreatic, prostate, breast cancer	(Allerstorfer et al., 2008; Ebert et al., 1995; Hanada et al., 2001; Metzner et al., 2011; Okada-Ban et al., 1999; Yoshimura et al., 1996)
FGF6	Colorectal, prostate, breast cancer	(Penault-Llorca et al., 1995; Ropiquet et al., 2000; Sheffer et al., 2009)
FGF7	Gastric, lung, ovarian cancer	(Shaoul et al., 2006; Yamayoshi et al., 2004; Yasuhara et al., 2005)
FGF8	Hepatocellular carcinoma, breast, prostate, bladder, lung cancer	(Berger et al., 1999; Gauglhofer et al., 2011; Tanaka et al., 1998; Yoshimura et al., 1996)
FGF9	Glioblastoma, prostate, non-small cell lung cancer	(Allerstorfer et al., 2008; Teishima et al., 2014; Yin et al., 2013)
FGF10	Pancreatic, prostate cancer	(Memarzadeh et al., 2007; Nomura et al., 2008)
FGF16	Ovarian cancer	(Basu et al., 2014)
FGF17	Hepatocellular carcinoma, prostate tumors	(Heer et al., 2004; Kwabi-Addo et al., 2004; Polnaszek et al., 2004)
FGF18	Melanoma, hepatocellular carcinoma, ovarian, colorectal, prostate, lung cancer	(Berger et al., 1999; Gauglhofer et al., 2011; Koneczny et al., 2014; Metzner et al., 2011; Wei et al., 2013)
FGF20	Colon, gastric, lung, ovarian endometrioid adenocarcinomas	(Chamorro et al., 2005; Jeffers et al., 2001; Wu et al., 2001)
FGF22	Non-melanoma skin cancer	(Jarosz et al., 2012)

Table S1, Related to Discussion. NSC12-bound canonical FGFs and cancer.

The table summarizes literature data pointing to a role of the various NSC12-targeted FGFs in different human tumors. For a more comprehensive description of the putative role(s) of the different members of the FGF family in human cancers see also (Beenken and Mohammadi, 2009; Brooks et al., 2012; Heinzle et al., 2011; Korc and Friesel, 2009; Lieu et al., 2011; Turner and Grose, 2010; Wesche et al., 2011).

SUPPLEMENTAL EXPERIMENTAL PROCEDURES

Reagents and cell cultures. Human recombinant FGF2 was from Tecnogen (Piana di Monteverna, Caserta, Italy), all other human recombinant FGFs were from PeproTech, anti-PTX3 rabbit polyclonal antibody from B. Bottazzi (Humanitas Clinical Institute, Rozzano, Italy) and alginic acid sodium salt from Sigma-Aldrich (Saint Louis, MO, USA).

^{15}N enriched human recombinant D2 domain (residues 147-249) from FGFR2 and human recombinant FGF2 (residues 1-154) were produced and purified by ASLA (Riga, Latvia. EU) as described below. NSC compounds were provided by Drug Synthesis and Chemistry Branch, Developmental Therapeutics Program, Division of Cancer Treatment and Diagnosis, National Cancer Institute (USA). Human recombinant VEGF-A_{165} was from R&D Systems (Minneapolis, MN, USA).

Human umbilical vein endothelial (HUVE) cells were used at passages I–IV and grown on plastic surface coated with porcine gelatin (Sigma-Aldrich) in M199 medium (Invitrogen, Carlsbad, CA, USA) supplemented with 20% fetal bovine serum (FBS) (Invitrogen), endothelial cell growth factor (100 μg/mL) (Sigma-Aldrich), and porcine heparin (100 μg/mL, Sigma-Aldrich). Murine prostate adenocarcinoma TRAMP-C2 cells were obtained from ATCC repository and maintained in DMEM supplemented with 10% heat inactivated FBS, 10 mM HEPES buffer, 0.5 mM 2-mercaptoethanol, 2.0 mM glutamine, 5 mg/L bovine insulin (Sigma-Aldrich) and 10 nM DHT. Murine Lewis lung carcinoma (LLC), B16-F10 melanoma and M5076 ovarian cancer cells (all cultured in DMEM *plus* 10% heat inactivated FBS), murine mammary carcinoma EO771 cells (cultured in DMEM *plus* 20% FBS) and prostate Panc02 cells (cultured in RPMI *plus* 10% FBS) were provided by R. Giavazzi (Istituto M. Negri, Milan, Italy). Murine TC-1 and C3 cells were kindly provided by L. Accardi (Istituto Superiore Sanità, Rome, Italy) and cultured as described (Accardi et al., 2014). Human LNCaP, DU145, H520 and HCC827 cell lines were obtained from ATCC and cultured in RPMI *plus* 10% FBS. KMS-11 cells were provided by C. Carlo-Stella (Humanitas Clinical Institute, Rozzano, Italy) and cultured in RPMI *plus* 10% FBS; Kato III and MDA-MB-361 cell lines were obtained from ATCC and cultured in DMEM *plus* 10% FBS.

Cells were maintained at low passage, returning to original frozen stocks every 3 to 4 months, and tested regularly for *Mycoplasma* negativity.

RT-PCR and RT-qPCR For mRNA expression analysis cells or organs harvested from TgN(Tie2-hPTX3) or wild type mice were processed and total RNA was extracted using TRIzol Reagent according to manufacturer's instructions (Invitrogen) and 2.0 μg of total RNA were retro-

transcribed with MMLV reverse transcriptase (Invitrogen) using random hexaprimers in a final 20 µl volume. Then, 1/10th of the reaction was analysed by semiquantitative RT-PCR using the following primers:
human PTX3, 5'-GTGCTCTCTGGTCTGCAGTG-3' (forward) and
5'-TCGTCCGTGGCTTGCAGCAG-3' (reverse);
murine FGFR1, 5'-GCTGACTCTGGCCTCTACGCT-3' (forward) and
5'-CAGGATCTGGACATACGGCAA-3' (reverse);
human FGFR1, 5'-GGGCTGGAATACTGCTACAA-3' (forward) and
5'-GCCAAAGTCTGCTATCTTCATC-3' (reverse);
murine CD31, 5'-CGGTTATGATGATGTTTCTGGA-3' (forward) and
5'-AAGGGAGGACACTTCCACTTCT-3' (reverse);
murine tubulin, 5'-TCACTGTGCCTGAACTTACC-3' (forward) and
5'-GGAACATAGCCGTAAACTGC-3' (reverse);
murine GAPDH, 5'-GAATTTGCCGTGAGTGGAGT-3' (forward) and
5'-GAAGGTCGGTGTGAACGGATT-3' (reverse).

For RT-qPCR determinations mRNA was prepared from organs of wild type and Tie2-hPTX3 mice and cDNA synthesized as described above. The following primers were used for qPCR:
murine FGF2, 5'- CCTTCCCACCAGGCCACTTAA-3' (forward) and
5'- GGTCCGTTTTGGATCCGAGTTT-3' (reverse);
murine FGF6, 5'-GCATCAGTGGAACACACGAGGA-3' (forward) and
5'-CAGTCTTCCTTTACTGTTCATGGC-3' (reverse);
murine FGF8, 5'- GAGCAACGGCAAAGGCAAGG-3' (forward) and
5'- CTCAACTACCCGCCCTTCAC-3' (reverse);
murine FGF10, 5'- ATCACCTCCAAGGAGATGTCCG-3' (forward) and
5'- CGGCAACAACTCCGATTTCCAC-3' (reverse);
murine FGF17, 5'- CCTAACCTTACCCTGTGCT-3' (forward) and
5'- GGTATTCACGGATTTGCCG-3' (reverse);
murine GAPDH, 5'-GAATTTGCCGTGAGTGGAGT-3' (forward) and
5'-GAAGGTCGGTGTGAACGGATT-3' (reverse).

Western blot analysis. Murine organs were washed in cold PBS and homogenized in RIPA buffer (1% Triton-X100, 0.2% BriJ, 1 mM sodium orthovanadate and protease inhibitors cocktail). CHO and MDA-MB-361 cells and TRAMP-C2 alginate plugs were homogenized in NP-40 lysis buffer

(1% NP-40, 20 mM Tris–HCl pH 8.0, 137 mM NaCl, 10% glycerol, 2.0 mM EDTA, 1.0 mM sodium orthovanadate and protease inhibitors cocktail). Protein concentrations were determined using the Bradford protein assay (Bio-Rad Laboratories, Milan, Italy, EU). Blotting analysis was performed using anti-PTX3 rabbit polyclonal antibody (from B. Bottazzi, Humanitas Clinical Institute, Rozzano, Italy), anti-phospho-FGFR1, anti-FGFR1, anti-FGFR2, anti-FGFR3, anti-FGFR4, anti-phospho-ERK1/2 (Santa Cruz Biotechnology, Santa Cruz, CA, USA) and anti-phosphotyrosine (Upstate, NY, USA). To normalize the amount of loaded proteins, all blots were probed with anti-α-tubulin or anti-β-actin antibodies (Sigma).

Lung endothelial cell isolation. Lungs from wild type or TgN(Tie2-hPTX3) were harvested, immersed in 5–10 ml of DMEM with 10% FBS and fragmented with a lancet to obtain a cell suspension. The suspensions were then incubated for 45 min at 37°C under constant rotation in the presence of 2 mg/ml of Collagenase D. Cell suspensions were then washed twice at 300 g for 15 min to inactivate Collagenase D and remove platelets and were finally passed through a 30 μm filter and labeled with a magnetic bead-conjugated anti-mouse CD31 antibody (Miltenyi Biotec, Bergisch-Gladbach, Germany, EU) for endothelial cell immunomagnetic sorting by the MiniMACS™ Separator system (Miltenyi Biotech). Labeling was performed according to the manufacturer's instructions. The endothelial phenotype of immunomagnetically sorted cells was confirmed by assessing *CD31* expression by RT-PCR and immunofluorescence analysis. Finally, endothelial cells were analyzed for the expression of *hPTX3* and *FGFR1* by RT-PCR and for the levels of phosphorylated FGFR1 by immunofluorescence analysis as described below.

Murine aorta ring assay. Mouse thoracic aorta rings, obtained from six weeks-old wild-type or TgN(Tie2-hPTX3) females, were placed on the bottom of 24 well-plates and coated with 30 μl of polymerizing fibrin solution (Ronca et al., 2010). After 5 min, wells were added with 600 μl of serum-free endothelial cell basal medium (Clonetics, Stillorgan, Ireland, EU) *plus* 10 μg/ml aprotinin in the presence of 10 ng/ml of FGF2 or VEGF-A. After 6 days, vessel sprouts were counted under a stereomicroscope.

Molecular Dynamics (MD) simulations of the ARPCA peptide. All-atom MD simulations were independently carried out on a simulation time scale of 200 ns for ARPCA in isolation, using an explicit water model. The fully extended conformation of the peptide was used to model the starting structure. The peptide was solvated in a tetrahedral solvation box large enough to contain at least 1.0 nm of water between the peptide and the box edge on all sides. All simulations and the analysis

of the trajectories were performed using the GROMACS software package using the GROMOS96 force field (Scott et al., 1999) and the SPC water model (Berendsen et al., 1987).

The system simulated in this part of the study was first energy relaxed with 2000 steps of steepest descent energy minimization followed by further 2000 steps of conjugate gradient energy minimization. The energy minimization was used to remove possible bad contacts from the initial structures. For each simulation, the system was equilibrated by 50 ps of MD runs with position restraints on the protein and ligand to allow relaxation of the solvent molecules. These first equilibration runs were followed by other 50 ps runs without position restraints on the solute. The first 10 ns of trajectory were not used in the subsequent analysis in order to minimize convergence artifacts. Equilibration of the trajectory was checked by monitoring the equilibration of quantities such as the RMSD with respect to the initial structure, internal protein energy, fluctuations calculated on different time-intervals. The electrostatic term was described by using the particle mesh Ewald algorithm. The LINCS (Hess et al., 1997) algorithm was used to constrain all bond lengths. For the water molecules the SETTLE algorithm (Miyamoto and Kollman, 1992) was used. A dielectric permittivity, $\epsilon = 1$, and a time step of 2 fs were used. All atoms were given an initial velocity obtained from a Maxwellian distribution at the desired initial temperature of 300K. The density of the system was adjusted performing the first equilibration runs at NPT condition by weak coupling to a bath of constant pressure (P_0 = 1 bar, coupling time τ_P = 0.5 ps) (Berendsen et al., 1984). In all simulations the temperature was maintained close to the intended values by weak coupling to an external temperature bath (Berendsen et al., 1984) with a coupling constant of 0.1 ps. The proteins and the rest of the system were coupled separately to the temperature bath. The structural cluster analysis was carried out using the method described by Daura and coworkers with a cutoff of 0.15nm (Daura et al., 1999).

Generation of a structural ARPCA:FGF2 complex model. The most representative structures of ARPCA obtained after cluster analysis of the trajectory were subjected to multiple docking runs on the surface of FGF2 (X-ray structure downloaded from the PDB: 1fq9.pdb) using the AUTODOCK (Morris et al., 2009) and ICM programs as described (Meli et al., 2006; Plescia et al., 2005). A consensus analysis of the results from the two docking programs was used to select the starting structured for successive MD runs. The representative of the most populated cluster obtained from the docking runs with both programs, corresponding to the minimum free energy structures in both cases, turned out to be very similar and was used for successive MD refinement. Two MD simulations (60 and 50 ns, respectively) were run using the same protocol as described above. Analysis of the statistical distribution of ARPCA/FGF2 interactions was carried out on the

combined trajectories (aminoacid side chains in contact for more than 75% of the simulation time are considered to define a stable interaction between FGF2 and ARPCA. A contact is defined if the center of mass of a certain residue is within 5.5Å (0.55nm) from the ligand). Consistent with previously published NMR-STD data, ARPCA contacts FGF2 *via* the methyl groups of residues Ala1 (contacting FGF2 residues Leu64, Ala66, Val72, where FGF2 residue numbering is from amino acid residue 1 as deduced from the cDNA sequence encoding the 155-residue form, used in the present NMR studies), Ala5 (contacting the aliphatic part of Arg106 and Gly70 chains) and of the acetyl capping group (contacting Leu64) (Leali et al., 2010). Attention was focused on the analysis of hydrogen-bonding, hydrophobic/aromatic and charge-charge interactions, as these represent the most common intermolecular forces in drug/receptor recognition. Hydrogen-bonding interactions were established by the backbone NH groups of ARPCA residues Ala1, Arg2 and Ala5 with FGF2-Glu105. A charge interaction was established between ARPCA-Arg2 and FGF2-Glu68 and one hydrophobic interaction was observed between ARPCA-Pro3 and FGF2-Leu107.

Pharmacophore model generation and screening-based lead identification. The results of the conformational analysis of the complexes, benchmarked against NMR data (Leali et al. 2010), were subjected to statistical analysis of contacts, hydrogen bonds, hydrophobic and electrostatic interactions. The statistically most relevant interactions were used as a template for pharmacophore design according to described procedures (Esteras-Chopo et al., 2008; Genoni et al., 2010; Meli et al., 2006). The pharmacophore generation and successive screening were carried out with the Discovery Studio suite of programs.

The pharmacophore model included the following features:

- Two hydrophobic functions mimicking the methyl groups of the capping acetyl group and Ala1;
- Two H-bond donor functions, located in a radius of 1.6 Å from the NH groups of Ala1 and Arg2;
- An aromatic/ cyclic-hydrophobic group located in the position of Pro3;
- An excluded volume comparable to the part of the peptide most in touch with the protein surface, specifically overlapping residues 1-3.

Such pharmacophore model was used to screen the NCI2003 database. Post filtering, using the Lipinski rules as a measure of drug likeness, allowed the selection of 25 possible hits.

The 480 Da compound 4,4,4-trifluoro-1-(3-hydroxy-10,13-dimethyl-2,3,4,7,8,9,11,12,14,15,16,17-dodecahydro-1H-cyclopenta[a]phenanthren-17-yl)-3-(trifluoromethyl)butane-1,3-diol (NSC172285, herewith named NSC12, **Figure 4A**) that efficiently prevented the formation of the HSPG/FGF2/FGFR1 complex was further characterized.

NSC12 was docked on the putative FGF2-ARPCA binding interface, using the same procedure described above. One preferential configuration was obtained and refined through a 100 ns long MD simulation in explicit water.

Molecular Dynamics (MD) refinement of the FGF2-NSC12 complex model. The MD trajectory was analyzed to identify the principal contacts between the NSC12 and the FGF2 surface. FGF2 amino acid side chains that contact NSC12 for more than 75% of the simulation time are considered to be engaged in a stable interaction with the ligand. A contact is defined if the center of mass of a certain residue is within 5.5Å (0.55nm) from the ligand. On the basis of this analysis, the butyl chain attached to the steroidic nucleus of NSC12 makes stable contacts with the hydrophobic patch defined by FGF2 residues Leu64, Ala66 and Val72. The two trifluoromethyl groups attached to Carbon-3 of the butyl chain optimally pack with this region. Moreover, the hydroxyl group on Carbon-1 (the butyl carbon atom also carrying the steroidic moiety, referred to the IUPAC name of the molecule) is engaged in a hydrogen bond with the side-chain of FGF2-Glu105 whereas the FGF2-Leu107 side-chain packs on rings A and B of the steroid (defined using conventional steroid nomenclature). These interactions and packing reflect the main functional and shape requirements used for the pharmacophore generation.

As expected given the different chemical nature of NSC12 compared to ARPCA, the small molecule drug is able to explore also different regions of the FGF2 surface. In particular, productive H-bonding interactions are observed during MD between the hydroxyl group on steroid Ring A with FGF2-Tyr115 and Ser152 whereas FGF2-Leu149 packs with Ring A of NSC12.

Overall, this first structural analysis indicates that NSC12 and ARPCA, while sharing part of the putative binding site, accounting for hydrophobic interactions as a consequence of pharmacophore design, may point to different regions of the FGF2 surface. In particular, NSC12 further extends to FGF2 region facing the D2-D3 linker and D2 domain.

Expression and Purification of ^{15}N-labelled D2 and FGF2. The uniformly ^{15}N-labeled D2 and FGF2 proteins were expressed and purified by ASLA according to previously optimized protocols (Hung et al., 2004a; Moy et al., 1995; Seddon et al., 1991). The expressed D2 domain comprises of 103 amino acids spanning residues 147–249 of the full length human FGFR2 (Hung et al., 2004a). Complete D2 and FGF2 chemical shift assignment was obtained starting from BMRB id: 5943 (Hung et al., 2004b) and our previous work (Pagano et al., 2012), respectively.

NMR studies of the FGF2/FGFR/NSC12 system. NMR samples contained 0.26 mM D2 and FGF2 in 20 mM phosphate buffer, 50 mM ammonium sulphate, pH 6.5. All NMR spectra were carried out on a 600 MHz DMX Bruker spectrometer at the temperature of 298K.

The FGFR D2 domain was used as a probe to report on the effects of NSC12 on FGF2/FGFR complex, thanks to its ability to fold into a stable structure in solution. In contrast, FGFR D3 domain alone does not adopt a stable three dimensional fold and the exchange between its various conformations causes severe line broadening, dramatically affecting the quality of NMR spectra. This holds valid even when the whole D2-D3 construct is considered (Herbert et al., 2013). D2 [^{1}H-^{15}N] HSQC spectra were recorded for the FGF2:D2 1:1 sample in the absence and in the presence of NSC12. Typically a sweep width of 13 ppm and 40 ppm, 1k x 128 data points were used in proton and nitrogen dimensions, respectively, for the 2D [1H-15N] HSQC spectra. Data were acquired and processed using Topspin (Bruker Biospin). The analysis was performed by means of Sparky (T. D. Goddard and D. G. Kneller, SPARKY3, University of California, San Francisco).

HSQC-based experiments were recorded to measure ^{15}N transverse R2 relaxation rates (Kay et al., 1989; Stone et al., 1992). Experiments were recorded using delays of 15.58, 31.17 (x2 times), 46.75, 77.92, 109.09, 124.67, 155.84, and 187.01 ms for both D2 and FGF2 proteins in complex, in the absence and in the presence of NSC12. Spectra were processed with nmrPipe (Delaglio et al., 1995), intensities were calculated with nmrView (One Moon Scientific Inc). R2 relaxation rates were determined by fitting peak intensities to single-exponential two parameter decay curves using the Rate Analysis tool inside nmrView. The Monte Carlo procedure was used to estimate the standard deviation of the data intensities. Average transverse relaxation rate values were calculated by selecting only residues in beta-strands elements. The average transverse relaxation rate values measured for D2 in complex with FGF2 decrease from 17.5±0.9 s^{-1} to 13.6±1.6 s^{-1} upon NSC12 addition (**Figure S4B,** *upper panel*). Similar figures were obtained for the FGF2 counterpart, whose average R2 values decreased from 15.4±0.5 s-1 to 13.3±1.4 s-1 upon NSC12 addition (**Figure S4B,** *lower panel*). The NMR results therefore indicate that NSC12 is able to perturb the FGF2/D2 complex, shifting the equilibrium towards the uncomplexed forms.

Surface Plasmon Resonance (SPR) analyses. A BIAcore X-100 apparatus (BIAcore Inc., Piscataway, NJ, USA) was used to set up the following experimental models.

Heparin chip: NSC12 was analyzed for its capacity to inhibit the binding of free FGF2 to immobilized heparin, prepared as described previously (Leali et al., 2010). Briefly, size-defined heparin (13.6 kD) was biotinylated on its reducing end and a flow cell of a CM3 sensor chip

(BIAcore Inc., Piscataway, NJ, USA) was activated with streptavidin. Then, biotinylated heparin was allowed to react with the streptavidin-coated sensor chip.

FGFR1 chip: NSC12 was analyzed for its capacity to inhibit the binding of free FGF2 to immobilized FGFR1. To this purpose, protein A (100 μg/ml in 10 mM sodium acetate, pH 4.8) was allowed to react with a flow cell of a CM5 sensor chip that was previously activated with a mixture of 0.2 M N-ethyl-N'-(3-dimethylaminopropyl)-carbodiimide hydrochloride and 0.05 M N-hydroxysuccinimide (35 μl, flow rate 10 μl/min). Following neutralization with 1.0 M ethanolamine (pH 8.5) (35 μl, flow rate 10 μl/min), recombinant human sFGFR1(IIIc)/Fc chimera (100 μg/ml) was allowed to react with the protein A-coated sensor chip. Then, a 30-sec. injection of a mixture (7 μl, flow rate 15 μl/min) of 0.2 M N-ethyl-N'-(3-dimethylaminopropyl)-carbodiimide hydrochloride and 0.05 M N-hydroxysuccinimide was performed, followed immediately by a 30-sec. injection of 1.0 M ethanolamine (pH 8.5) (7 μl, flow rate 15 μl/min). These experimental conditions allowed the immobilization of ~0.003 pmol/mm^2 of sFGFR1(IIIc)/Fc chimera. Protein A-coated sensorchip was used as a negative control and for blank subtraction.

FGF chips: NSC12 was analyzed for its capacity to directly bind to immobilized FGFs. To this purpose, FGFs (20 μg/ml in 10 mM sodium acetate, pH 6.0) were allowed to react with a flow cell of a CM5 sensor chip that was previously activated with a mixture of 0.2 M N-ethyl-N'-(3-dimethylaminopropyl)-carbodiimide hydrochloride and 0.05 M N-hydroxysuccinimide (35 μl, flow rate 10 μl/min). FGFs were immobilized with a density of approximately (1.42 ± 0.3)x10^{10} molecule/mm^2 to the CM5 chip (see the following paragraph). After ligand immobilization, matrix neutralization was performed with 1.0 M ethanolamine (pH 8.5) (35 μl, flow rate 10 μl/min) and the activated/deactivated dextran was used as reference (control) system.

Increasing concentrations of NSC12 (ranging between 29 and 150 μM) were injected over the FGF-coated sensor chip and the response was recorded as a function of time tracking the SPR intensity change upon binding progression. Injection lasted for 4 min (flow rate 30 μl/min) to allow NSC12 association to immobilized FGF2 and was followed by 10 min of dissociation; each run was performed in 3% DMSO in PBS and the sensor chip was regenerated with 10 mM NaOH. The equilibrium (plateau) values of the SPR sensorgrams were used to build the binding isotherms (dose-response curves) displayed, after normalization, in Figure 5D (top panel) of the main text. Binding isotherm points were fitted with the Langmuir equation for monovalent binding. This allowed to evaluate the mass surface dissociation constant, K_d, and the scaling parameter that relates the SPR signal with the extent of binding, as the free parameters of the fitting. The errors on these

parameters were assigned as a result of the fitting algorithm (95% confidence bounds). The best-fitting procedure was performed with the SigmaPlot 11.0 software package (Systat Software Inc.).
Additional sensor chips were prepared with other FGF family members (all from PeproTech) as described for FGF2 to test the binding capacity of NSC12 by SPR analysis.

Determination of the surface density of FGF2 and of NSC12 on the chips used for biosensing experiments. The equilibrium amount of NSC12 bound to the FGF2 chip functionalized with (1.42 ± 0.3)x10^{10} molecule/mm^2 after exposure to a 100 μM NSC12 solution was determined taking in account that the BIAcore X-100 is calibrated to give 1000 RU for 1 ng/mm^2 of molecules adsorbed on the sensor surface, having care to use the unfunctionalized chip as baseline/reference. The evaluated NSC12 surface density bound to the FGF2 resulted $\wp$=(1.28 ± 0.3)x10^{10} molecule/mm^2.

COntact Angle MOlecular REcognition (CONAMORE).

A. The Young-Dupré equation for Δγ. The nanomechanical transduction parameter, $\Delta\gamma$, is related to the interfacial tensions and contact angles of the reference and of the specific systems by an *ad hoc* version of the the Young-Dupré equation:

$$\Delta\gamma = \gamma - \gamma^0 = \gamma^0 \cos\theta^0 - \gamma\cos\theta$$

where θ^0 and θ are the contact angles of the control and of the specific systems, respectively, and γ^0 and γ are the solution-surrounding phase interfacial tensions of the control and of the active systems, respectively. This equation allows to directly calculate $\Delta\gamma$ after determining θ by sessile drop contact angle experiments, and γ by pendant drop experiments, as briefly described in the following. For full details see (Olivero et al., 2010).

B. Experiments and data analysis. The experiments were implemented from previously described procedures (Maiolo et al., 2012; Olivero et al., 2010). CONAMORE chips were prepared analogously to the ones prepared for SPR, but without the assistance of microfluidics. Analogously, the NSC12 solutions and doses that were ran in CONAMORE experiments were the same ran in SPR experiments.
Sessile drop measurements were carried out with a CAM 200 tensiometer (KSV Instruments, Finland) equipped with a Navitar camera at room temperature and under cyclohexane light phase by following described protocols (Olivero et al., 2010). The mean θ for each solution droplet was evaluated by three independent replicates deposited in three different zones of the same chip and the SD of the mean taken as the error. Before performing a sessile drop experiment with a new solution, the chip was regenerated by a quick immersion in glycine pH 4.0 (to remove the bound ligands) and sequential washing with PBS and Milli-Q water.

Determination of solution-cyclohexane interfacial tension, γ, was performed through the standard pendant drop method. The pendant drop images were analyzed by the Young–Laplace equation (KSV CAM Optical Contact Angle and Pendent Drop Surface Tension Software 4.04) and γ evaluated. γ values were determined as the mean of three independent replicates and the errors determined as the SD of the mean.

Contact angle measurements were also performed on substrates after a treatment in urea in order to unfold the immobilized FGF2. The functionalized chips were immersed in 6 M urea for 30 minutes and then accurately rinsed in PBS and water.

HSPG/FGF/FGFR1 mediated cell-cell adhesion assay. This assay was performed as described (Leali et al., 2001) with minor modifications. Briefly, wild-type CHO-K1 cells were seeded in 24-well plates at 150,000 cells/cm^2. After 24 hours, cell monolayers were washed with PBS and incubated with 3% glutaraldehyde in PBS for 2 hours at 4°C. Fixation was stopped with 0.1 M glycine and cells were washed extensively with PBS. Then, A745-CHO-flg-1A-*luc* cells (50,000 cells/cm^2) were added to CHO-K1 monolayers in serum-free medium *plus* 10 mM EDTA with or without 30 ng/mL of the FGF under test in the absence or presence of increasing concentrations of the different NSC compounds. After 2 hours of incubation at 37°C, unattached cells were removed by washing twice with PBS, and A745-CHO-flg-1A-*luc* bound to the CHO-K1 monolayer were solubilized and luciferase activity was quantified. All experiments were performed in triplicate.

In vitro immunofluorescence analysis. HUVE cells were seeded in Ibidi® μ-Slide 8 wells (Ibidi, Martinsried, Germany, EU) at a density of 30,000 cells/cm^2, starved in 2.5% FBS for 24 hours and stimulated for 20 minutes with 30 ng/ml of FGF2 in the absence or presence of NSC12 or NSC21. Following stimulation, cells were washed twice in PBS, fixed in cold acetone for 5 minutes and permeabilized with 0.2% Triton-X100 in PBS for 2 minutes at RT. After washing in PBS, cells were blocked for 10 minutes at RT in 1% BSA and then incubated with rabbit anti-pFGFR1 (Tyr766h, code: sc-16309-R, Santa Cruz Biotechnology) or rabbit anti-FGFR1 (C-15, code: sc-121, Santa Cruz Biotechnology) antibodies for 1 hour at RT. After washing in PBS, cells were incubated with AlexaFluor 594-conjugated anti-rabbit antibody (Invitrogen) and DAPI for 30 minutes at RT. Finally, cells were examined under a Zeiss Fluorescence Axiovert 200M microscope (Carl Zeiss, Milan, Italy, EU). Specificity of anti-FGFR1 and anti-pFGFR1(Tyr766) antibody immunoreaction was confirmed on FGF2-stimulated FGFR1$^{-/-}$ murine embryonic stem (ES) cells stably transfected with human FGFR1 (hFGFR1) or with the Y766F-hFGFR1 mutant cDNAs (Dell'Era at al., 2003) (see **Figure S1B**).

Endothelial cell sprouting assay. HUVE cell spheroid aggregates were prepared in 20% methylcellulose medium, embedded in fibrin gel, and stimulated with FGF2 or VEGF-A (both at 30 ng/ml) *plus* 5% FBS in the absence or presence of 1 μM NSC12 or NSC21. Formation of radially growing cell sprouts was observed during the next 24 hours, photographed at 200x magnification using an Axiovert 200M microscope and counted.

Viable cell counting. Cells were cultured under appropriate conditions for 48 or 72 hours. Propidium iodide staining (Immunostep, Salamanca, SP, EU) was used to detect PI^- viable cells by flow cytometry. Absolute cell counts were obtained by the counting function of the MACSQuant® Analyzer (Miltenyi Biotec).

Cell cycle analysis. Cells were cultured under appropriate conditions for 48 hours, fixed in 70% ethanol and then stained with 40 μg/ml PI (SigmaAldrich). Cell cycle was measured using the MACSQuant® Analyzer (Miltenyi Biotec) and analyzed using the FlowJo vX.0.7 software (Tree Star, Inc., Ashland, OR, USA).

MTT assay. KATO III cells were plated at 10^4 cells/well in 96 well-plates in RPMI medium *plus* 1% FBS. After 24 hours cells were treated with different FGFs (30 ng/ml) in the absence or presence of an optimal dose of NSC12 (1.0 or 3.0 μM) or NSC21. After 72 hours the MTT assay was performed according to manufacturer's instructions. The optical density (OD) was determined using a plate reader at a test wavelength of 595 nm and a reference wavelength of 630 nm (Bai et al., 2010).

Chick embryo chorioallantoic membrane (CAM) assay. Gelatin sponges (Gelfoam; Pfizer) containing vehicle, FGF2 or VEGF-A (both at 5 pmoles/embryo) in the absence or presence of 0.5 to 5 pmoles of NSC12 or NSC21 were placed on the CAM of fertilized white leghorn chicken eggs at day 11 of incubation. At day 14, newly formed blood microvessels converging toward the implant were counted by two observers in a double-blind fashion at 5x magnification under a stereomicroscope (STEMI-SR, x2/0.12; Zeiss) as described (Ribatti et al., 2006).

Generation of transgenic TgN(Tie2-hPTX3) mice. The Tie2-hPTX3 lentiviral transfer vector was obtained by cloning the *hPTX3* cDNA (GenBank accession n° X63613) into the original Tie2p/e-GFP vector (De Palma et al., 2003). Concentrated VSV.G-pseudotyped lentiviral vector stocks were produced and titered (De Palma et al., 2003) to generate transgenic TgN(Tie2-hPTX3) mice as

described (Lois et al., 2002). Briefly, female C57BL/6 mice were superovulated with a combination of pregnant mare serum and human chorionic gonadotropin (Lois et al., 2002). Embryos were collected from each female and microinjected into the perivitelline space with 10-100 pl of 10^8 TU/ml vector stock of Tie2-hPTX3 lentiviral particles. Tie2-hPTX3 manipulated embryos were immediately implanted into the oviduct of pseudopregnant CD1 mice. Pups were genotyped for the presence of *hPTX3* and lentiviral vector backbone:
lentiviral backbone, 5'-CGCTATGTGGATACGCTGCTTTAA-3' (forward) and 5'-GCTGACAGGTGGTGGCAATGCCCC-3' (reverse).
Vector-positive mice were bred to test germ-line transmission of the transgene. DNA was also used to quantify the vector copy number in founder (F0) and F1 mice by real time PCR as described (De Palma et al., 2003). F1 mice were crossed to obtain F2-3 progenies. F2-3 littermates were used in all the experiments described.
Procedures involving animals and their care conformed with institutional guidelines that comply with national and international laws and policies.

Matrigel plug angiogenesis assay. Six week-old female wild-type or transgenic TgN(Tie2-hPTX3) C57BL/6 mice were injected s.c. with 400 µl of Matrigel containing PBS or 180 ng of FGF2. After 7 days, pellets were processed for total RNA extraction or immunofluorescence analysis and the vascular response was quantified by evaluation of the levels of expression of the endothelial marker CD31 as previously described (Coltrini et al., 2013).

Murine s.c. alginate implant assay. Twelve week-old wild type or TgN(Tie2-hPTX3) C57BL/6 male mice were injected s.c. with 450 µl of 3% (w/v) sodium alginate solution (alginic acid dissolved in LPS-free PBS) containing $3x10^6$ TRAMP-C2 cells. After 14 days, alginate plugs were harvested, weighted and processed for total RNA extraction and histological analysis.
The tumor cell proliferative and vascular responses were quantified by evaluation of the levels of expression of the cell proliferation marker *cyclin D1* and of the endothelial markers *CD31* by quantitative RT-PCR. To this purpose, total RNA was extracted from alginate plugs using TRIzol Reagent according to manufacturer's instructions (Invitrogen). Purified total RNA was dissolved in 100 µl of RNase free water and contaminating DNA was digested using DNase, following the protocol reported in DNase1 Amplification Grade kit (Sigma-Aldrich). Five µl of total RNA were retrotranscribed with MMLV reverse transcriptase (Invitrogen) using random hexaprimers in a final 20 µL volume. Quantitative PCR was performed with a Biorad iCycler iQ™ Real-Time PCR Detection System using a iQ™ SYBR Green Supermix (Biorad) according to manufacturer's

instructions. Each PCR reaction was performed in triplicate on one plate and fluorescence data were recorded using iCycler software (BioRad). Relative expression levels were normalized in respect to *18S r*RNA levels or to *GAPDH* mRNA levels.

The following primers were used:

murine cyclin D1, 5'-AGACCATTCCCTTGACTGC-3' (forward) and
5'-AAGCAGTTCCATTTGCAGC-3' (reverse);

murine CD31, 5'-CGGTTATGATGATGTTTCTGGA-3' (forward) and
5'-AAGGGAGGACACTTCCACTTCT-3' (reverse);

murine 18S, 5'-GGTGGTGCATGGCCGTTCTTAG-3' (forward) and
5'-GCTAACGCCACTTGTCCCTCTA-3' (reverse);

murine GAPDH, 5'-GAATTTGCCGTGAGTGGAGT-3' (forward) and
5'-GAAGGTCGGTGTGAACGGATT-3' (reverse).

Similarly, DU145, H520 or HCC827 cells ($5x10^6$ cells/implant) were embedded in 3% alginate and injected s.c. in Nu/Nu mice. Two weeks after injection mice were treated i.p. with NSC12, NSC21 or vehicle (DMSO) every other day for one week. Plugs were removed, weighted and processed for histological analyses. For immunofluorescence analysis of alginate plugs see the "Histological analyses" paragraph.

In vivo NSC12 toxicity studies. Eight week-old wild type C57BL/6 mice were treated i.p. with 7.5 or 10 mg/kg of NSC12 every other day for two weeks. During this period, animals were weighted for body weight variation analysis. At the end of treatment, whole blood and serum were harvested from mice treated with 7.5 mg/kg of NSC12 and analysed for blood components, biochemical serum parameters and circulating levels of hormonal FGFs. The serum levels of hormonal FGFs (including FGF19, FGF21 and FGF23) were assessed by ELISA kits (Uscn Life Science Inc., Wuhan, PRC, Asia) according to the manufacturer's instructions. Untreated mice were used as reference/control.

Heterotopic tumor models. Nine week-old wild-type and transgenic TgN(Tie2-hPTX3) male mice were injected s.c. with $5x10^6$ TRAMP-C2 cells. Six-week old wild-type, TgN(Tie2-hPTX3) or $PTX3^{-/-}$ female mice were injected s.c. with $5x10^4$ LLC cells or $1x10^4$ B16-F10 cells. DU145 and H520 cells were injected at $5x10^6$ cells/implant in 7 week-old Nu/Nu mice and Nu/Nu females, respectively. TC-1 ($1x10^5$) and C3 ($5x10^5$) cells were injected s.c. in C57BL/6 female mice. All injections were performed in 200 µl total volume of PBS into the dorsolateral flank. Treatment was

performed by i.p. injection (in DMSO) or oral gavage [in DMSO/water (1:1)] of NSC12 or NSC21 (both at 5 or 7.5 mg/kg) in 100 µl final volume.
Tumors were measured in two dimensions and tumor volume was calculated according to the formula $V=(D \times d^2)/2$, where D and d are the major and minor perpendicular tumor diameters, respectively (Euhus et al., 1986).

Transgenic bone marrow transplantation experiments. Six week-old C57BL/6 male mice were treated i.p. for 4 days with busulfan (25 mg/kg) (Lewis et al., 2013). The fifth day, depleted mice were transplanted i.v. with 100 µl of saline containing $15x10^6$ bone marrow cells derived from the femurs of 6 week-old TgN(Tie2-hPTX3) or TgN(Tie2-GFP) mice. Bone marrow depletion and reconstitution were checked by cytofluorimetric analysis of the peripheral blood $CD45^+$ cell population on mice before busulfan treatment, 4 days after busulfan treatment and 4 weeks after reconstitution. The chimerism was checked by PCR on the gDNA obtained from the peripheral blood of transplanted mice using the target lentiviral sequences present in the TgN strains [primers: *lentiviral backbone*, CGCTATGTGGATACGCTGCTTTAA (forward) and GCTGACAGGTGGTGGCAATGCCCC (reverse)]. Six weeks after bone marrow transplantation, mice were injected s.c. into the dorsolateral flank with $5x10^6$ TRAMP-C2 cells in 200 µl total volume of PBS. Tumors were measured in two dimensions and tumor volume was calculated according to the formula $V=(D \times d^2)/2$, where D and d are the major and minor perpendicular tumor diameters, respectively. At the end of the experiment tumors were removed and processed for histological and PCR analyses.

Orthotopic tumor models. EO771 cells were injected ($2x10^5$ in 50 µl of PBS) in the mammary fat pad of 7 week-old wild-type and TgN(Tie2-hPTX3) female mice, tumor growth was measured in two dimensions and Kaplan-Meier survival curve was determined. Panc02-*luc* cells ($3x10^5$ in 30 µl of PBS) were injected into the pancreas of 7 week-old wild-type and TgN(Tie2-hPTX3) female mice. Tumor growth was imaged with IVIS Lumina III and the survival Kaplan-Meier estimator curve was obtained with GraphPad Prism software.

Double TgN(Tie2-hPTX3)/TRAMP transgenic and $PTX3^{-/-}$ mice. TRAMP mice (C57BL/6-Tg(TRAMP)8247Ng/J) (Greenberg et al., 1995) were purchased from The Jackson Laboratory (Bar Harbor, ME, USA), bred crossing homozygous females with C57BL/6J wild type males and heterozygous TRAMP males were used for experimental procedures.

For the generation of double transgenic TgN(Tie2-hPTX3)/TRAMP mice, homozygous TRAMP females were crossed with Tie2-hPTX3 males to generate first generation hemyzigous-TRAMP/Tie2-hPTX3 animals. These mice were crossed to generate second generation homozygous-TRAMP/Tie2-hPTX3 female breeders. Homozygous-TRAMP/Tie2-hPTX3 females were crossed with Tie2-hPTX3 males to generate the heterozygous TgN(Tie2-hPTX3)/TRAMP males that were used for the experimental procedures.
PTX3 *knock out* mice were provided by C. Garlanda (Istituto Clinico Humanitas, Milan, Italy) and maintained as described (Garlanda et al., 2002).

Murine prostate histopathological analysis. The genitourinary apparatus was removed from wild-type, TRAMP or TgN(Tie2-hPTX3)/TRAMP mice and paraffin-embedded. Anterior prostate sections (7 μm thick) were stained with H&E or immunostained with anti-PTX3 and anti-Ki67 antibodies and evaluated for specific histological abnormalities. The full prostate section was acquired at 20x magnification with a Zeiss Axiovert 200M microscope (Carl Zeiss, Milan, Italy, EU) using the "Mosaic Tool" and the quantification of the pathological areas was performed with the ImagePro Plus software. Also, the number of pathological adenomers was determined and pathological areas were graded as described (Shappell et al., 2004).

Metastasis models. B16-F10 ($3x10^4$) or M5076 ($1x10^4$) cells in 100 μl of PBS were injected into the tail vein of 7 week-old wild-type and TgN(Tie2-hPTX3) mice. After 3 weeks, lungs or livers were harvested, weighted, formalin-fixed and the number of metastases were counted under a dissecting microscope. Lungs and livers were then processed for immunohistochemical analysis. Luciferase expressing B16-F10-*luc* cells ($3x10^4$ in 100 μl of PBS) were injected into the tail vein of six week-old wild-type C57BL/6 mice and animals were treated every other day for two weeks by i.p. injection (in DMSO) with NSC12 or NSC21 (7.5 mg/kg) in 100 μl final volume. Live imaging was performed with IVIS Lumina III (PerkinElmer). At the end of the experiment (4 weeks after tumor injection) lungs were harvested, weighted and metastatic foci were counted. For spontaneous metastases, EO771 cells ($5x10^5$) were injected into the mammary fat pad of C57BL/6 female mice and tumors were resected when reached the 8 mm x 13 mm size. After one week of recovery mice were treated i.p. every other day for four weeks with vehicle, NSC12 or NSC21 (7.5 mg/kg) in 100 μl final volume (Hiratsuka et al., 2011). At the end of the experimental procedure mice were sacrificed, lungs harvested and macro-metastases were counted.

Histological analyses. Samples were either embedded in OCT compound and immediately frozen or fixed in formalin and embedded in paraffin.

For immunofluorescence analysis, cryostat sections (5 μm thick) were air dried and fixed with acetone (5 min at 4°C). After blocking with 1% BSA in PBS for 10 minutes, sections were incubated for 1 hour at room temperature with primary antibodies [rabbit anti-FGFR1 (Santa Cruz Biotechnology), rabbit anti-pFGFR1 (Santa Cruz Biotechnology), rat anti-mouse CD31 (BD Biosciences Pharmingen, San Diego, CA, USA), rabbit anti-human PTX3, rat anti-mouse Ki67 (Dako, Milano, Italy, EU), rabbit anti-human Ki67 (Invitrogen)]. After washing with PBS containing 0.05% Tween 20, sections were incubated with the appropriate Alexa Fluor 488 or Alexa Fluor 594-conjugated secondary antibody (Invitrogen). TdT-mediated dUTP nick end labeling (TUNEL) staining (Roche, Milano, Italy, EU) was performed according to the manufacturer's instructions in sections (2 μm thick) from formalin-fixed, paraffin-embedded alginate plugs, and dead cells were detected in the green channel. After mounting in a drop of anti-bleaching mounting medium containing DAPI (Vectashield, Vector Laboratories, Burlingame, CA, USA), sections were examined under a Zeiss Fluorescence Axiovert 200M (Carl Zeiss) microscope. Omission of the primary antibody (Ctrl-) confirms the specificity of FGFR1 and pFGFR1 immunostaining of alginate plugs (Figure below).

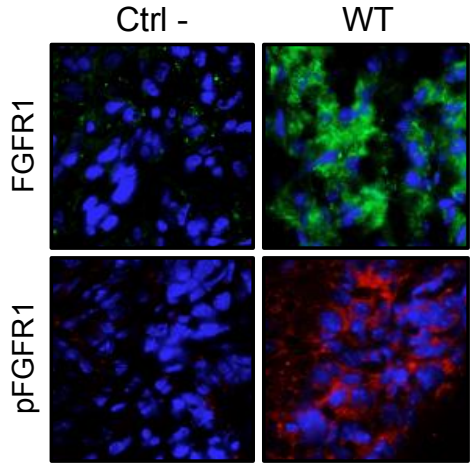

Representative images of the negative controls (Ctrl-) obtained by omitting the primary antibody for the panels shown in the main text on Figure 2.

Formalin-fixed, paraffin-embedded samples were sectioned at a thickness of 2 μm, dewaxed, hydrated, and stained with hematoxylin and eosin (H&E) or processed for immunohistochemistry with rabbit anti-human PTX3, rat anti-mouse CD31 (BD Pharmingen), rat anti-mouse Ki67 (Dako) antibodies. Positive signal was revealed by 3,3'-diaminibenzidine (Roche) or ferangi blue (Biocare Medical, Concord, CA, USA) stainings. Sections were finally counterstained with Carazzi's hematoxylin before analysis by light microscopy. Images were acquired with the automatic high-resolution scanner Aperio System (Leica Biosystems, Wetzlar, Germany, EU).

Image analysis was carried out using the open-source ImageJ software (http://rsb.info.nih.gov/ij/).

Statistical analyses. Statistical analyses were performed using the statistical package Prism 5 (GraphPad Software) run on a Macintosh Pro personal computer (Apple Computers).
Student's *t* test for unpaired data (2-tailed) was used to test the probability of significant differences between two groups of samples. For more than two groups of samples, data were statistically analyzed with a 1-way analysis of variance, and individual group comparisons were evaluated by the Bonferroni multiple comparison test. Tumor volume data were statistically analyzed with a 2-way analysis of variance, and individual group comparisons were evaluated by the Bonferroni correction. Differences were considered significant when $P < 0.05$.

SUPPLEMENTAL REFERENCES

Accardi, L., Paolini, F., Mandarino, A., Percario, Z., Di Bonito, P., Di Carlo, V., Affabris, E., Giorgi, C., Amici, C., and Venuti, A. (2014). In vivo antitumor effect of an intracellular single-chain antibody fragment against the E7 oncoprotein of human papillomavirus 16. International journal of cancer. J. Int. Cancer *134*, 2742-2747.

Allerstorfer, S., Sonvilla, G., Fischer, H., Spiegl-Kreinecker, S., Gauglhofer, C., Setinek, U., Czech, T., Marosi, C., Buchroithner, J., Pichler, J., *et al*. (2008). FGF5 as an oncogenic factor in human glioblastoma multiforme: autocrine and paracrine activities. Oncogene *27*, 4180-4190.

Arao, T., Ueshima, K., Matsumoto, K., Nagai, T., Kimura, H., Hagiwara, S., Sakurai, T., Haji, S., Kanazawa, A., Hidaka, H., *et al*. (2013). FGF3/FGF4 amplification and multiple lung metastases in responders to sorafenib in hepatocellular carcinoma. Hepatology *57*, 1407-1415.

Bai, A., Meetze, K., Vo, N. Y., Kollipara, S., Mazsa, E. K., Winston, W. M., Weiler, S., Poling, L. L., Chen, T., Ismail, N. S., *et al*. (2010). GP369, an FGFR2-IIIb-specific antibody, exhibits potent antitumor activity against human cancers driven by activated FGFR2 signaling. Cancer Res. *70*, 7630-7639.

Basu, M., Mukhopadhyay, S., Chatterjee, U., and Roy, S. S. (2014). FGF16 promotes invasive behavior of SKOV-3 ovarian cancer cells through activation of mitogen-activated protein kinase (MAPK) signaling pathway. J. Biol. Chem. *289*, 1415-1428.

Beenken, A., and Mohammadi, M. (2009). The FGF family: biology, pathophysiology and therapy. Nature reviews. Drug Discov. *8*, 235-253.

Berendsen, H. J. C., Grigera, J. R., and Straatsma, T. P. (1987). The Missing Term in Effective Pair Potentials. J. Phys. Chem.-US *91*, 6269-6271.

Berendsen, H. J. C., Postma, J. P. M., Vangunsteren, W. F., Dinola, A., and Haak, J. R. (1984). Molecular-Dynamics with Coupling to an External Bath. J. Chem. Phys. *81*, 3684-3690.

Berger, W., Setinek, U., Mohr, T., Kindas-Mugge, I., Vetterlein, M., Dekan, G., Eckersberger, F., Caldas, C., and Micksche, M. (1999). Evidence for a role of FGF-2 and FGF receptors in the proliferation of non-small cell lung cancer cells. J. Int. Cancer *83*, 415-423.

Brooks, A. N., Kilgour, E., and Smith, P. D. (2012). Molecular pathways: fibroblast growth factor signaling: a new therapeutic opportunity in cancer. Clin. Cancer Res. *18*, 1855-1862.

Cao, Z., Ding, B. S., Guo, P., Lee, S. B., Butler, J. M., Casey, S. C., Simons, M., Tam, W., Felsher, D. W., Shido, K., *et al*. (2014). Angiocrine factors deployed by tumor vascular niche induce B cell lymphoma invasiveness and chemoresistance. Cancer Cell *25*, 350-365.

Chamorro, M. N., Schwartz, D. R., Vonica, A., Brivanlou, A. H., Cho, K. R., and Varmus, H. E. (2005). FGF-20 and DKK1 are transcriptional targets of beta-catenin and FGF-20 is implicated in cancer and development. EMBO J. *24*, 73-84.

Coltrini, D., Di Salle, E., Ronca, R., Belleri, M., Testini, C., and Presta, M. (2013). Matrigel plug assay: evaluation of the angiogenic response by reverse transcription-quantitative PCR. Angiogenesis *16*, 469-477.

Daura, X., Gademann, K., Jaun, B., Seebach, D., van Gunsteren, W. F., and Mark, A. E. (1999). Peptide folding: When simulation meets experiment. Angew. Chem. Int. Edit. *38*, 236-240.

De Palma, M., Venneri, M. A., Roca, C., and Naldini, L. (2003). Targeting exogenous genes to tumor angiogenesis by transplantation of genetically modified hematopoietic stem cells. Nature Med. *9*, 789-795.

Delaglio, F., Grzesiek, S., Vuister, G. W., Zhu, G., Pfeifer, J., and Bax, A. (1995). NMRPipe: a multidimensional spectral processing system based on UNIX pipes. J. Biomol. NMR *6*, 277-293.

Dell'Era, P., Ronca, R., Coco, L., Nicoli, S., Metra, M., and Presta, M. (2003). Fibroblast growth factor receptor-1 is essential for in vitro cardiomyocyte development. Circ Res. *93*, 414-420.

Ebert, M., Yokoyama, M., Friess, H., Kobrin, M. S., Buchler, M. W., and Korc, M. (1995). Induction of platelet-derived growth factor A and B chains and over-expression of their receptors in human pancreatic cancer. J. Int. Cancer *62*, 529-535.

Esteras-Chopo, A., Morra, G., Moroni, E., Serrano, L., Lopez de la Paz, M., and Colombo, G. (2008). A molecular dynamics study of the interaction of D-peptide amyloid inhibitors with their target sequence reveals a potential inhibitory pharmacophore conformation. J. Mol. Biol. *383*, 266-280.

Euhus, D. M., Hudd, C., LaRegina, M. C., and Johnson, F. E. (1986). Tumor measurement in the nude mouse. J. Surg. Oncol. *31*, 229-234.

Garlanda, C., Hirsch, E., Bozza, S., Salustri, A., De Acetis, M., Nota, R., Maccagno, A., Riva, F., Bottazzi, B., Peri, G., *et al*. (2002). Non-redundant role of the long pentraxin PTX3 in anti-fungal innate immune response. Nature *420*, 182-186.

Gauglhofer, C., Sagmeister, S., Schrottmaier, W., Fischer, C., Rodgarkia-Dara, C., Mohr, T., Stattner, S., Bichler, C., Kandioler, D., Wrba, F., *et al*. (2011). Up-regulation of the fibroblast growth factor 8 subfamily in human hepatocellular carcinoma for cell survival and neoangiogenesis. Hepatology *53*, 854-864.

Genoni, A., Morra, G., Merz, K. M., Jr., and Colombo, G. (2010). Computational study of the resistance shown by the subtype B/HIV-1 protease to currently known inhibitors. Biochemistry *49*, 4283-4295.

Ghaneh, P., Kawesha, A., Evans, J. D., and Neoptolemos, J. P. (2002). Molecular prognostic markers in pancreatic cancer. J. Hepatobiliary Pancreat. Surg. *9*, 1-11.

Greenberg, N. M., DeMayo, F., Finegold, M. J., Medina, D., Tilley, W. D., Aspinall, J. O., Cunha, G. R., Donjacour, A. A., Matusik, R. J., and Rosen, J. M. (1995). Prostate cancer in a transgenic mouse. Proc. Natl. Acad. Sci. U S A *92*, 3439-3443.

Hanada, K., Perry-Lalley, D. M., Ohnmacht, G. A., Bettinotti, M. P., and Yang, J. C. (2001). Identification of fibroblast growth factor-5 as an overexpressed antigen in multiple human adenocarcinomas. Cancer Res. *61*, 5511-5516.

Heer, R., Douglas, D., Mathers, M. E., Robson, C. N., and Leung, H. Y. (2004). Fibroblast growth factor 17 is over-expressed in human prostate cancer. J. Pathol. *204*, 578-586.

Heinzle, C., Sutterluty, H., Grusch, M., Grasl-Kraupp, B., Berger, W., and Marian, B. (2011). Targeting fibroblast-growth-factor-receptor-dependent signaling for cancer therapy. Expert Opin. Ther. Targets *15*, 829-846.

Herbert, C., Schieborr, U., Saxena, K., Juraszek, J., De Smet, F., Alcouffe, C., Bianciotto, M., Saladino, G., Sibrac, D., Kudlinzki, D., *et al*. (2013). Molecular mechanism of SSR128129E, an extracellularly acting, small-molecule, allosteric inhibitor of FGF receptor signaling. Cancer Cell *23*, 489-501.

Hess, B., Bekker, H., Berendsen, H. J. C., and Fraaije, J. G. E. M. (1997). LINCS: A linear constraint solver for molecular simulations. J. Comput. Chem. *18*, 1463-1472.

Hiratsuka, S., Duda, D. G., Huang, Y., Goel, S., Sugiyama, T., Nagasawa, T., Fukumura, D., and Jain, R. K. (2011). C-X-C receptor type 4 promotes metastasis by activating p38 mitogen-activated protein kinase in myeloid differentiation antigen (Gr-1)-positive cells. Proc. Natl. Acad. Sci. U S A *108*, 302-307.

Hung, K. W., Kumar, T. K., Chi, Y. H., Chiu, I. M., and Yu, C. (2004a). Molecular cloning, overexpression, and characterization of the ligand-binding D2 domain of fibroblast growth factor receptor. Biochem. Biophys. Res. Commun. *317*, 253-258.

Hung, K. W., Kumar, T. K., and Yu, C. (2004b). 1H, (13)C and (15)N chemical shift assignments of the D2 domain of the fibroblast growth factor receptor. J. Biomol. NMR *30*, 99-100.

Jarosz, M., Robbez-Masson, L., Chioni, A. M., Cross, B., Rosewell, I., and Grose, R. (2012). Fibroblast growth factor 22 is not essential for skin development and repair but plays a role in tumorigenesis. PloS One *7*, e39436.

Jeffers, M., Shimkets, R., Prayaga, S., Boldog, F., Yang, M., Burgess, C., Fernandes, E., Rittman, B., Shimkets, J., LaRochelle, W. J., and Lichenstein, H. S. (2001). Identification of a novel human fibroblast growth factor and characterization of its role in oncogenesis. Cancer Res. *61*, 3131-3138.

Kay, L. E., Torchia, D. A., and Bax, A. (1989). Backbone dynamics of proteins as studied by 15N inverse detected heteronuclear NMR spectroscopy: application to staphylococcal nuclease. Biochemistry *28*, 8972-8979.

Koneczny, I., Schulenburg, A., Hudec, X., Knofler, M., Holzmann, K., Piazza, G., Reynolds, R., Valent, P., and Marian, B. (2014). Autocrine fibroblast growth factor 18 signaling mediates Wnt-dependent stimulation of CD44-positive human colorectal adenoma cells. Mol. Carcinog. [Epub ahead of print].

Korc, M., and Friesel, R. E. (2009). The role of fibroblast growth factors in tumor growth. Curr. Cancer Drug Targets *9*, 639-651.

Kwabi-Addo, B., Ozen, M., and Ittmann, M. (2004). The role of fibroblast growth factors and their receptors in prostate cancer. Endoc. Relat. Cancer *11*, 709-724.

Leali, D., Belleri, M., Urbinati, C., Coltrini, D., Oreste, P., Zoppetti, G., Ribatti, D., Rusnati, M., and Presta, M. (2001). Fibroblast growth factor-2 antagonist activity and angiostatic capacity of sulfated Escherichia coli K5 polysaccharide derivatives. J. Biol. Chem. *276*, 37900-37908.

Leali, D., Bianchi, R., Bugatti, A., Nicoli, S., Mitola, S., Ragona, L., Tomaselli, S., Gallo, G., Catello, S., Rivieccio, V., *et al*. (2010). Fibroblast growth factor 2-antagonist activity of a long-pentraxin 3-derived anti-angiogenic pentapeptide. J. Cell. Mol. Med. *14*, 2109-2121.

Lewis, C. A., Manning, J., Barr, C., Peake, K., Humphries, R. K., Rossi, F., and Krieger, C. (2013). Myelosuppressive conditioning using busulfan enables bone marrow cell accumulation in the spinal cord of a mouse model of amyotrophic lateral sclerosis. PloS One *8*, e60661.

Lieu, C., Heymach, J., Overman, M., Tran, H., and Kopetz, S. (2011). Beyond VEGF: inhibition of the fibroblast growth factor pathway and antiangiogenesis. Clin. Cancer Res. *17*, 6130-6139.

Lois, C., Hong, E. J., Pease, S., Brown, E. J., and Baltimore, D. (2002). Germline transmission and tissue-specific expression of transgenes delivered by lentiviral vectors. Science *295*, 868-872.

Maiolo, D., Mitola, S., Leali, D., Oliviero, G., Ravelli, C., Bugatti, A., Depero, L. E., Presta, M., and Bergese, P. (2012). Role of nanomechanics in canonical and noncanonical pro-angiogenic ligand/VEGF receptor-2 activation. J. Am. Chem. Soc. *134*, 14573-14579.

Meli, M., Pennati, M., Curto, M., Daidone, M. G., Plescia, J., Toba, S., Altieri, D. C., Zaffaroni, N., and Colombo, G. (2006). Small-molecule targeting of heat shock protein 90 chaperone function: rational identification of a new anticancer lead. J. Med. Chem. *49*, 7721-7730.

Memarzadeh, S., Xin, L., Mulholland, D. J., Mansukhani, A., Wu, H., Teitell, M. A., and Witte, O. N. (2007). Enhanced paracrine FGF10 expression promotes formation of multifocal prostate adenocarcinoma and an increase in epithelial androgen receptor. Cancer Cell *12*, 572-585.

Metzner, T., Bedeir, A., Held, G., Peter-Vorosmarty, B., Ghassemi, S., Heinzle, C., Spiegl-Kreinecker, S., Marian, B., Holzmann, K., Grasl-Kraupp, B., *et al*. (2011). Fibroblast growth factor receptors as therapeutic targets in human melanoma: synergism with BRAF inhibition. J. Invest. Dermatol. *131*, 2087-2095.

Miyamoto, S., and Kollman, P. A. (1992). Settle - an Analytical Version of the Shake and Rattle Algorithm for Rigid Water Models. J. Comput. Chem. *13*, 952-962.

Morris, G. M., Huey, R., Lindstrom, W., Sanner, M. F., Belew, R. K., Goodsell, D. S., and Olson, A. J. (2009). AutoDock4 and AutoDockTools4: Automated Docking with Selective Receptor Flexibility. J. Comput. Chem. *30*, 2785-2791.

Moy, F. J., Seddon, A. P., Campbell, E. B., Bohlen, P., and Powers, R. (1995). 1H, 15N, 13C and 13CO assignments and secondary structure determination of basic fibroblast growth factor using 3D heteronuclear NMR spectroscopy. J. Biomol. NMR *6*, 245-254.

Nomura, S., Yoshitomi, H., Takano, S., Shida, T., Kobayashi, S., Ohtsuka, M., Kimura, F., Shimizu, H., Yoshidome, H., Kato, A., and Miyazaki, M. (2008). FGF10/FGFR2 signal induces cell migration and invasion in pancreatic cancer. Br. J. Cancer *99*, 305-313.

Okada-Ban, M., Moens, G., Thiery, J. P., and Jouanneau, J. (1999). Nuclear 24 kD fibroblast growth factor (FGF)-2 confers metastatic properties on rat bladder carcinoma cells. Oncogene *18*, 6719-6724.

Olivero, G., Maiolo, D., Leali, D., Federici, S., Depero, L. E., Presta, M., Mitola, S., and Bergese, P. (2010). Nanoliter contact angle probes tumor angiogenic ligand-receptor protein interactions. Biosens. Bioelectron. *26*, 1571-1575.

Pagano, K., Torella, R., Foglieni, C., Bugatti, A., Tomaselli, S., Zetta, L., Presta, M., Rusnati, M., Taraboletti, G., Colombo, G., and Ragona, L. (2012). Direct and allosteric inhibition of the FGF2/HSPGs/FGFR1 ternary complex formation by an antiangiogenic, thrombospondin-1-mimic small molecule. PloS One *7*, e36990.

Penault-Llorca, F., Bertucci, F., Adelaide, J., Parc, P., Coulier, F., Jacquemier, J., Birnbaum, D., and deLapeyriere, O. (1995). Expression of FGF and FGF receptor genes in human breast cancer. International journal of cancer. J. Int. Cancer *61*, 170-176.

Plescia, J., Salz, W., Xia, F., Pennati, M., Zaffaroni, N., Daidone, M. G., Meli, M., Dohi, T., Fortugno, P., Nefedova, Y., *et al*. (2005). Rational design of shepherdin, a novel anticancer agent. Cancer Cell *7*, 457-468.

Polnaszek, N., Kwabi-Addo, B., Wang, J., and Ittmann, M. (2004). FGF17 is an autocrine prostatic epithelial growth factor and is upregulated in benign prostatic hyperplasia. Prostate *60*, 18-24.

Ribatti, D., Nico, B., Vacca, A., and Presta, M. (2006). The gelatin sponge-chorioallantoic membrane assay. Nature Protocols *1*, 85-91.

Roidl, A., Foo, P., Wong, W., Mann, C., Bechtold, S., Berger, H. J., Streit, S., Ruhe, J. E., Hart, S., Ullrich, A., and Ho, H. K. (2010). The FGFR4 Y367C mutant is a dominant oncogene in MDA-MB453 breast cancer cells. Oncogene 29, 1543-1552.

Ronca, R., Alessi, P., Coltrini, D., Di Salle, E., Giacomini, A., Leali, D., Corsini, M., Belleri, M., Tobia, C., Garlanda, C., *et al*. (2013a). Long pentraxin-3 as an epithelial-stromal fibroblast growth factor-targeting inhibitor in prostate cancer. J. Pathol. *230*, 228-238.

Ronca, R., Benzoni, P., Leali, D., Urbinati, C., Belleri, M., Corsini, M., Alessi, P., Coltrini, D., Calza, S., Presta, M., and Dell'Era, P. (2010). Antiangiogenic activity of a neutralizing human single-chain antibody fragment against fibroblast growth factor receptor 1. Mol. Cancer Ther. *9*, 3244-3253.

Ronca, R., Di Salle, E., Giacomini, A., Leali, D., Alessi, P., Coltrini, D., Ravelli, C., Matarazzo, S., Ribatti, D., Vermi, W., and Presta, M. (2013b). Long Pentraxin-3 Inhibits Epithelial-Mesenchymal Transition in Melanoma Cells. Mol. Cancer Ther. *12*, 2760-2771.

Ropiquet, F., Giri, D., Kwabi-Addo, B., Mansukhani, A., and Ittmann, M. (2000). Increased expression of fibroblast growth factor 6 in human prostatic intraepithelial neoplasia and prostate cancer. Cancer Res. *60*, 4245-4250.

Ruotsalainen, T., Joensuu, H., Mattson, K., and Salven, P. (2002). High pretreatment serum concentration of basic fibroblast growth factor is a predictor of poor prognosis in small cell lung cancer. Cancer Epidemiol. Biomarkers Prev. *11*, 1492-1495.

Scott, W. R. P., Hunenberger, P. H., Tironi, I. G., Mark, A. E., Billeter, S. R., Fennen, J., Torda, A. E., Huber, T., Kruger, P., and van Gunsteren, W. F. (1999). The GROMOS biomolecular simulation program package. J. Phys. Chem. A *103*, 3596-3607.

Seddon, A., Decker, M., Muller, T., Armellino, D., Kovesdi, I., Gluzman, Y., and Bohlen, P. (1991). Structure/activity relationships in basic FGF. Ann. NY Acad. Sci. *638*, 98-108.

Shain, S. A., Saric, T., Ke, L. D., Nannen, D., and Yoas, S. (1996). Endogenous fibroblast growth factor-1 or fibroblast growth factor-2 modulate prostate cancer cell proliferation. Cell Growth Differ. *7*, 573-586.

Shaoul, R., Eliahu, L., Sher, I., Hamlet, Y., Miselevich, I., Goldshmidt, O., and Ron, D. (2006). Elevated expression of FGF7 protein is common in human gastric diseases. Biochem. Biophys. Res, Commun. *350*, 825-833.

Shappell, S. B., Thomas, G. V., Roberts, R. L., Herbert, R., Ittmann, M. M., Rubin, M. A., Humphrey, P. A., Sundberg, J. P., Rozengurt, N., Barrios, R., *et al*. (2004). Prostate pathology of genetically engineered mice: definitions and classification. The consensus report from the Bar Harbor meeting of the Mouse Models of Human Cancer Consortium Prostate Pathology Committee. Cancer Res. *64*, 2270-2305.

Sheffer, M., Bacolod, M. D., Zuk, O., Giardina, S. F., Pincas, H., Barany, F., Paty, P. B., Gerald, W. L., Notterman, D. A., and Domany, E. (2009). Association of survival and disease progression with chromosomal instability: a genomic exploration of colorectal cancer. Proc. Natl. Acad. Sci. U S A *106*, 7131-7136.

Soria, J. C., DeBraud, F., Bahleda, R., Adamo, B., Andre, F., Dientsmann, R., Delmonte, A., Cereda, R., Isaacson, J., Litten, J., *et al*. (2014). Phase I/IIa study evaluating the safety, efficacy, pharmacokinetics, and pharmacodynamics of lucitanib in advanced solid tumors. Ann. Oncol. *25*, 2244-2251.

Stone, M. J., Fairbrother, W. J., Palmer, A. G., 3rd, Reizer, J., Saier, M. H., Jr., and Wright, P. E. (1992). Backbone dynamics of the Bacillus subtilis glucose permease IIA domain determined from 15N NMR relaxation measurements. Biochemistry *31*, 4394-4406.

Tai, A. L., Sham, J. S., Xie, D., Fang, Y., Wu, Y. L., Hu, L., Deng, W., Tsao, G. S., Qiao, G. B., Cheung, A. L., and Guan, X. Y. (2006). Co-overexpression of fibroblast growth factor 3 and epidermal growth factor receptor is correlated with the development of nonsmall cell lung carcinoma. Cancer *106*, 146-155.

Tanaka, A., Furuya, A., Yamasaki, M., Hanai, N., Kuriki, K., Kamiakito, T., Kobayashi, Y., Yoshida, H., Koike, M., and Fukayama, M. (1998). High frequency of fibroblast growth factor (FGF) 8 expression in clinical prostate cancers and breast tissues, immunohistochemically demonstrated by a newly established neutralizing monoclonal antibody against FGF 8. Cancer Res. *58*, 2053-2056.

Teishima, J., Yano, S., Shoji, K., Hayashi, T., Goto, K., Kitano, H., Oka, K., Nagamatsu, H., and Matsubara, A. (2014). Accumulation of FGF9 in prostate cancer correlates with epithelial-to-mesenchymal transition and induction of VEGF-A expression. Anticancer Res. *34*, 695-700.

Turner, N., and Grose, R. (2010). Fibroblast growth factor signalling: from development to cancer. Nature reviews. Cancer *10*, 116-129.

Wei, W., Mok, S. C., Oliva, E., Kim, S. H., Mohapatra, G., and Birrer, M. J. (2013). FGF18 as a prognostic and therapeutic biomarker in ovarian cancer. J. Clin. Invest. *123*, 4435-4448.

Wesche, J., Haglund, K., and Haugsten, E. M. (2011). Fibroblast growth factors and their receptors in cancer. Biochem. J. *437*, 199-213.

Wu, R., Zhai, Y., Fearon, E. R., and Cho, K. R. (2001). Diverse mechanisms of beta-catenin deregulation in ovarian endometrioid adenocarcinomas. Cancer Res. *61*, 8247-8255.

Yamanaka, Y., Friess, H., Buchler, M., Beger, H. G., Uchida, E., Onda, M., Kobrin, M. S., and Korc, M. (1993). Overexpression of acidic and basic fibroblast growth factors in human pancreatic cancer correlates with advanced tumor stage. Cancer Res. *53*, 5289-5296.

Yamayoshi, T., Nagayasu, T., Matsumoto, K., Abo, T., Hishikawa, Y., and Koji, T. (2004). Expression of keratinocyte growth factor/fibroblast growth factor-7 and its receptor in human lung cancer: correlation with tumour proliferative activity and patient prognosis. J. Pathol. *204*, 110-118.

Yasuda, K., Torigoe, T., Mariya, T., Asano, T., Kuroda, T., Matsuzaki, J., Ikeda, K., Yamauchi, M., Emori, M., Asanuma, H., *et al*. (2014). Fibroblasts induce expression of FGF4 in ovarian cancer stem-like cells/cancer-initiating cells and upregulate their tumor initiation capacity. Lab. Invest. *94*, 1355-1369.

Yasuhara, T., Okamoto, A., Kitagawa, T., Nikaido, T., Yoshimura, T., Yanaihara, N., Takakura, S., Tanaka, T., Ochiai, K., and Ohtake, Y. (2005). FGF7-like gene is associated with pericentric inversion of chromosome 9, and FGF7 is involved in the development of ovarian cancer. Int. J. Oncol. *26*, 1209-1216.

Yin, Y., Betsuyaku, T., Garbow, J. R., Miao, J., Govindan, R., and Ornitz, D. M. (2013). Rapid induction of lung adenocarcinoma by fibroblast growth factor 9 signaling through FGF receptor 3. Cancer Res. *73*, 5730-5741.

Yoshida, M. C., Wada, M., Satoh, H., Yoshida, T., Sakamoto, H., Miyagawa, K., Yokota, J., Koda, T., Kakinuma, M., Sugimura, T., and et al. (1988). Human HST1 (HSTF1) gene maps to chromosome band 11q13 and coamplifies with the INT2 gene in human cancer. Proc. Natl. Acad. Sci. U S A *85*, 4861-4864.

Yoshimura, K., Eto, H., Miyake, H., Hara, I., Arakawa, S., and Kamidono, S. (1996). Messenger ribonucleic acids for fibroblast growth factors and their receptor in bladder and renal cell carcinoma cell lines. Cancer Lett. *103*, 91-97.

Zaharieva, B. M., Simon, R., Diener, P. A., Ackermann, D., Maurer, R., Alund, G., Knonagel, H., Rist, M., Wilber, K., Hering, F., *et al*. (2003). High-throughput tissue microarray analysis of 11q13 gene amplification (CCND1, FGF3, FGF4, EMS1) in urinary bladder cancer. J. Pathol. *201*, 603-608.